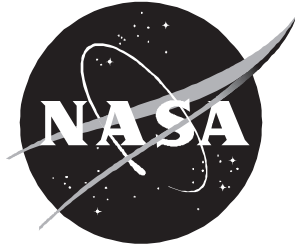


NASA/TP-1999-209718



Unstructured Grid Viscous Flow Simulation Over High-Speed Research Technology Concept Airplane at High-Lift Conditions

Farhad Ghaffari
Langley Research Center, Hampton, Virginia

November 1999

The NASA STI Program Office . . . in Profile

Since its founding, NASA has been dedicated to the advancement of aeronautics and space science. The NASA Scientific and Technical Information (STI) Program Office plays a key part in helping NASA maintain this important role.

The NASA STI Program Office is operated by Langley Research Center, the lead center for NASA's scientific and technical information. The NASA STI Program Office provides access to the NASA STI Database, the largest collection of aeronautical and space science STI in the world. The Program Office is also NASA's institutional mechanism for disseminating the results of its research and development activities. These results are published by NASA in the NASA STI Report Series, which includes the following report types:

- **TECHNICAL PUBLICATION.** Reports of completed research or a major significant phase of research that present the results of NASA programs and include extensive data or theoretical analysis. Includes compilations of significant scientific and technical data and information deemed to be of continuing reference value. NASA counterpart of peer-reviewed formal professional papers, but having less stringent limitations on manuscript length and extent of graphic presentations.
- **TECHNICAL MEMORANDUM.** Scientific and technical findings that are preliminary or of specialized interest, e.g., quick release reports, working papers, and bibliographies that contain minimal annotation. Does not contain extensive analysis.
- **CONTRACTOR REPORT.** Scientific and technical findings by NASA-sponsored contractors and grantees.
- **CONFERENCE PUBLICATION.** Collected papers from scientific and technical conferences, symposia, seminars, or other meetings sponsored or co-sponsored by NASA.
- **SPECIAL PUBLICATION.** Scientific, technical, or historical information from NASA programs, projects, and missions, often concerned with subjects having substantial public interest.
- **TECHNICAL TRANSLATION.** English-language translations of foreign scientific and technical material pertinent to NASA's mission.

Specialized services that complement the STI Program Office's diverse offerings include creating custom thesauri, building customized databases, organizing and publishing research results . . . even providing videos.

For more information about the NASA STI Program Office, see the following:

- Access the NASA STI Program Home Page at <http://www.sti.nasa.gov>
- Email your question via the Internet to help@sti.nasa.gov
- Fax your question to the NASA STI Help Desk at (301) 621-0134
- Telephone the NASA STI Help Desk at (301) 621-0390
- Write to:
NASA STI Help Desk
NASA Center for AeroSpace Information
7121 Standard Drive
Hanover, MD 21076-1320

NASA/TP-1999-209718



Unstructured Grid Viscous Flow Simulation Over High-Speed Research Technology Concept Airplane at High-Lift Conditions

Farhad Ghaffari
Langley Research Center, Hampton, Virginia

National Aeronautics and
Space Administration

Langley Research Center
Hampton, Virginia 23681-2199

November 1999

The use of trademarks or names of manufacturers in this report is for accurate reporting and does not constitute an official endorsement, either expressed or implied, of such products or manufacturers by the National Aeronautics and Space Administration.

Available from:

NASA Center for AeroSpace Information (CASI)
7121 Standard Drive
Hanover, MD 21076-1320
(301) 621-0390

National Technical Information Service (NTIS)
5285 Port Royal Road
Springfield, VA 22161-2171
(703) 605-6000

Available electronically at the following URL address: <http://techreports.larc.nasa.gov/ltrs>

Abstract

Numerical viscous solutions based on an unstructured grid methodology are presented for a candidate high-speed civil transport configuration, designated as the Technology Concept Airplane (TCA), within the High-Speed Research (HSR) program. The numerical results are obtained on a representative TCA high-lift configuration that consisted of the fuselage and the wing, with deflected full-span leading-edge and trailing-edge flaps. Typical on- and off-surface flow structures, computed at high-lift conditions appropriate for the takeoff and landing, indicated features that are generally plausible. Reasonable surface pressure correlations between the numerical results and the experimental data are obtained at free-stream Mach number $M_\infty = 0.25$ and Reynolds number based on \bar{c} $R_{\bar{c}} = 8 \times 10^6$ for moderate angles of attack of 9.7° and 13.5° . However, above and below this angle-of-attack range, the correlation between computed and measured pressure distributions starts to deteriorate over the examined angle-of-attack range. The predicted longitudinal aerodynamic characteristics are shown to correlate very well with existing experimental data across the examined angle-of-attack range. An excellent agreement is also obtained between the predicted lift-to-drag ratio and the experimental data over the examined range of flow conditions.

Introduction

In recent years there has been considerable progress made to advance the state-of-the-art unstructured grid methodology for simulating nonlinear viscous flows over complete aircraft configurations. The primary interest for advancing such a technology is the inherent advantage and flexibility with which a tetrahedral mesh can conform to a complex surface geometry, along with the associated ease in generating the corresponding flow-field volume grids. In addition to the versatilities associated with the unstructured grid generation, complementary technology advancements in digital computers, both in terms of speed and memory, have also promoted notable progress in the unstructured grid algorithm developments for simulating complex, three-dimensional, nonlinear viscous flows. Despite this encouraging progress, however, for various reasons, the application of this technology is not widespread among the general user community, in particular for viscous flow simulation. One may account for this lack of popularity because this is an emerging technology, and thus is not validated/calibrated for complex flow characteristics often associated with realistic aerospace vehicles across flight speed regimes. As a result, the unstructured grid technology is presently undergoing various stages of validation/calibration for different types of flows and configurations from fundamental (refs. 1 to 3) to complex (refs. 4 and 5) configuration problems. Such

benchmark analyses are critical to building confidence and credibility in the numerical predictions for different classes of configurations and flow problems.

One such method among various emerging unstructured grid technologies is the Tetrahedral Unstructured Software System (TetrUSS) (ref. 6) developed at Langley Research Center (LaRC). TetrUSS has four separate software packages: the flow solver USM3Dns, the grid generator VGRIDns, the surface geometry discretizer GRIDTOOL, and the solution postprocessor VPLOT3D. The Euler version of TetrUSS has been extensively validated and calibrated for a variety of complex flows and configurations (refs. 7 to 11). In addition, a new adaptive unstructured grid Euler method has recently been developed (ref. 12) and coupled with TetrUSS. In reference 12, the applicability of this new grid adaptive method has been successfully demonstrated to capture complex flow characteristics for a variety of aerospace configurations at flow conditions ranging from low speed to supersonic Mach number. In the past few years, however, the viscous capabilities of TetrUSS, in particular the flow solver USM3Dns and the grid generator VGRIDns, have been maturing for simulating complex flows around geometrically complex configurations (ref. 4). One main feature of the flow solver USM3Dns is the coupling of the Reynolds Average Navier-Stokes (RANS) equations with a wall function to simulate the boundary layer viscous flows. This

approximation for viscous flow simulation is made primarily to alleviate the large computer memory requirements associated with solving the RANS equations within the thin near-wall tetrahedral cells in the viscous sublayer region. The results from the application of this method for predicting the shock that induces separated flows at transonic high Reynolds number conditions for the ONERA M6 wing are presented in reference 1. In this report, the predicted surface pressure coefficients that are based on the wall function approximation are shown to correlate very well with experimental data, as well as with predictions from the full Navier-Stokes analysis. Furthermore, the predicted surface flow patterns, computed with the wall function, are also reported to be comparable to those that are computed based on the full Navier-Stokes formulation.

The study assesses the applicability of this method for predicting the complex separated flows associated with a High-Speed Civil Transport (HSCT) configuration, designated as the Technology Concept Airplane (TCA) within NASA's High-Speed Research (HSR) program at low-speed, high-lift conditions. Such complex separated flows, emanating either from surface discontinuities (e.g., wing sharp leading edges and side edges of the deflected wing trailing-edge flaps) or from a smooth or round region of a surface (e.g., flap hinge lines and blunt wing leading edge) are considered among the most challenging aerodynamic problems to simulate numerically. Although this particular method has not been validated/calibrated for such applications, attempts will be made in the solution analyses to demonstrate the method's strengths and weaknesses in predicting some of the major flow physics associated with this class of aerodynamic problem. The accuracy assessments of the predicted results will be gauged through comparisons with the available experimental data obtained at LaRC. Figures in this report appear in color at <http://techreports.larc.nasa.gov/ltrs/PDF/1999/tp/NASA-99-tp209718.pdf>.

Symbols

b	reference span, 78.757 in.
\bar{c}	reference chord, 56.972 in.
C_D	drag coefficient, $\text{Drag}/(q_\infty S_{\text{ref}})$

C_L	lift coefficient, $\text{Lift}/(q_\infty S_{\text{ref}})$
C_m	pitching-moment coefficient, $\text{Pitching moment}/(q_\infty S_{\text{ref}} \bar{c})$
C_p	pressure coefficient, $(p - p_\infty)/q_\infty$
M_∞	free-stream Mach number
p	static pressure, lb/in^2
p_∞	free-stream static pressure, lb/in^2
q_∞	free-stream dynamic pressure, lb/in^2
$R_{\bar{c}}$	Reynolds number based on \bar{c}
S_{ref}	reference area, 3060.0 in^2
v^*	wall-friction velocity, $\sqrt{\tau_w/\rho}$, in/sec
X, Y, Z	geometry reference coordinate system
y	normal distance from viscous wall, in.
y^+	inner-law variable, yv^*/ν
α	angle of attack, deg
μ	viscosity, $\text{lb}\cdot\text{sec}/\text{in}^2$
ν	kinematic viscosity, μ/ρ , in^2/sec
ρ	density, slug/in^3
τ_w	wall shear stress, lb/in^2

Abbreviations:

CFD	computational fluid dynamics
CFL	Courant, Friedrichs, Lewy number
CPU	central processing unit
FDS	flux difference splitting
FS	fuselage station
HSCT	High-Speed Civil Transport
HSR	high-speed research

IGES	Initial Graphics Exchange Specification
LaRC	Langley Research Center
NAS	Numerical Aerospace Simulation
PVA	primary vortex attachment
RANS	Reynolds Average Navier-Stokes
SV	secondary vortex
SVSL	secondary vortex separation line
TCA	Technology Concept Airplane
TetrUSS	Tetrahedral Unstructured Software System

Experimental Data

The wind tunnel experiment was performed in the Langley 14- by 22-Foot Subsonic Tunnel. The test was conducted with a 0.05-scale model of the TCA configuration, mounted on the floor of the tunnel, by using a strut apparatus, as shown in figure 1. The primary objective of the test was to obtain low-speed aerodynamic performance data for the complete TCA configuration in the takeoff and landing flight modes, which are generally referred to as the high-lift conditions. In addition to testing the complete TCA model, a few experimental runs also were made with a more geometrically simplified version of the configuration, primarily to obtain data for computational fluid dynamics (CFD) method prediction assessments. This simplified geometry consisted of only the fuselage and the wing, incorporating different leading- and trailing-edge flap deflections and excluding the engine components.

In addition to the overall force and moment measurements, the model was instrumented for static pressure measurements over the wing upper and lower surfaces at various spanwise and chordwise stations on the starboard side. A schematic planform view of the TCA configuration, along with the spanwise pressure port locations to be used in the present analysis and correlations with computational predictions, are shown in figure 2. The measured longitudinal aerodynamic data were subsequently corrected to account for wind tunnel wall interference effects by using Heyson's wall correction method (ref. 13). Correc-

tions were made also for the presence of the mounting-strut apparatus. The latter correction was based on the incremental effects of the measured forces and moments obtained in an earlier test conducted in the same tunnel on a 0.06-scale model of the same class vehicle, that is, the Boeing-designed Reference H configuration.

The experimental data were analyzed prior to the development of the computational matrix to identify a candidate configuration and an appropriate range of angles of attack that are representative of the high-lift conditions for takeoff and landing. This analysis led to the selection of a simplified TCA configuration that consisted of the fuselage and wing, with fully deflected leading-edge flaps of 30° and fully deflected trailing-edge flaps of 10° . The numerical solid model representation of the selected configuration is shown in figure 3 from different perspective views. Subsequently, the angles of attack of 5.7° , 9.7° , 13.5° , 17.2° , and 21° at $M_\infty = 0.25$ and $R_{\bar{c}} = 8 \times 10^6$ were selected for the computational analysis.

Computational Approach and Attributes

Flow Solver

All numerical results presented in this report were computed by using the flow solver USM3Dns (ref. 1). The time-dependent, three-dimensional RANS equations were solved to simulate the flow within the computational domain discretized by tetrahedral-mesh elements. USM3Dns is based on the cell centered, finite volume approach and uses an upwind-biased flux-difference-splitting (FDS) scheme (ref. 14) for spatial discretization of the primitive flow variables. Flow solutions are advanced by the implicit time integration approach (ref. 15), with convergence accelerated to steady state by local time stepping. All computations presented in this report were obtained with the second-order FDS scheme, *minmod* limiter, and 10-stage subiterations for implicit Gauss-Seidel time stepping.

For turbulent viscous flow simulation, the method solves the RANS equations along with the Spalart-Allmaras (ref. 16) one-equation turbulence model. The viscous flow solutions are then coupled with a

law-of-the-wall function, derived by Spalding (as published in ref. 17) to approximate the flow within the sublayer of the turbulent boundary layer (ref. 18). This boundary layer approximation provides a significant reduction in the overall memory requirement by eliminating the grids normally needed for resolving the boundary layer flow within the turbulent inner sub-layer (i.e., typically $y^+ < \approx 20$ to 50). Such an approximation also improves the solution convergence characteristics caused by the reduced stretching of the near-the-wall cells, which generally adds stiffness to the numerical analysis. However, due to the inherent limitations of the wall function approximation, there are also genuine concerns about the accuracy of the numerical solutions in predicting the detailed flow physics, such as flow separation from a smooth surface. To predict this type of flow separation, which occurs because of the adverse pressure gradient within the boundary layer, requires the integration of the RANS equations to the configuration solid surface. As a result, efforts will be made in the present numerical analyses to examine the ability of the method in predicting such a flow characteristic.

Computational Grid Discretization and Attributes

The wing full-span leading-edge flaps are deflected to 30° , and both trailing-edge flap segments (inboard and outboard) are deflected to 10° (fig. 3). This particular configuration, although geometrically simple, is thought to generate all major external flow physics associated with the takeoff and landing conditions experienced by the complete TCA vehicle. As a result, this baseline configuration, along with the corresponding experimental data, is chosen for the present numerical analysis. The baseline TCA geometry is defined parametrically for the wing and the fuselage in a format known as Initial Graphics Exchange Specification (IGES), reference 19. This geometry definition served as the database for all subsequent grid generation processes. GRIDTOOL (ref. 20) is primarily used to discretize the geometry into various surface patches which are then fed into VGRIDns (refs. 21 and 22) to generate the initial surface triangulation by the advancing front method. The initial surface triangles, also referred to as the initial advancing front, are then read back into the GRIDTOOL program for projection onto the initial database defined in IGES format. The projection process of the initial front onto the initial database is required to preserve

the proper surface curvature within the interior of a given patch. Finally, the projected surface triangles and the defined far-field boundary patches are used by VGRIDns to generate the complete volume grid (i.e., viscous and inviscid) within the computational domain, along with the corresponding grid and face connectivity files for the flow solver. The flow-field grid generated for the present analysis effectively used the newly developed feature of VGRIDns, allowing stretching of the grids in any direction on the surface or in the field. The present computational grid is stretched in the spanwise direction along the wing leading and trailing edges. The grid-stretching rate factor is strategically chosen for various regions of the configuration to efficiently model the local geometric features or the expected flow physics. The grid-stretching rate factor is varied anywhere between 1.05 to 1.25 for different regions, and generally, the higher rate factor is applied to the field grid in the radial direction beyond the viscous advancing-front layers.

The far-field boundary faces of the computational domain, which is shaped like a rectangular parallelepiped, are located at about $20\bar{c}$ upstream and downstream, $18\bar{c}$ spanwise, and $9\bar{c}$ above and below the numerical model (fig. 4(a)). For reference, $\bar{c} = 56.972$ in., and the origin of the reference coordinate system ($X = 0$, $Y = 0$, and $Z = 0$) is defined to coincide with the fuselage nose apex. The overall configuration body length is about 195.6 in. in 0.05-scale model dimension. In the present numerical analysis, the external flow field is assumed to be symmetrical about the configuration plane of symmetry; thus, only half the configuration is modeled. Near-field and close-up views of the surface triangles and the grids in the plane of symmetry are shown in figures 4(b) through 4(f) from various vantage points. Suitable grids are distributed on the surface to capture either the various curvatures and discontinuities (e.g., flap hinge lines, trailing-edge-flap gaps, leading and trailing edges, and wing-fuselage juncture) and the expected flow characteristics. The computational model consisted of about 60000 surface boundary triangles, about 870000 tetrahedral cells within the viscous boundary layer region, and about 780000 cells in the inviscid computational domain. The computational grid contained about 18 to 21 tetrahedra cells within the boundary layer (see representative in the plane of symmetry, fig. 4(b)) with the first grid spacing sized normal to the surface to yield $y^+ \approx 20$ at approximately midfuselage body length.

Because of the wall function implementation, the USM3Dns slip velocity boundary condition is used on the configuration's solid surfaces. Furthermore, the characteristic boundary condition is invoked on the computational domain far-field boundaries, along with the outflow plane. The free-stream boundary condition is specified for the inflow plane to initiate the computation.

Numerical Results and Analyses

The computations were initiated with the focus on the $\alpha = 13.5^\circ$ case to develop an application procedure that could be applied to obtain consistent numerical results for the other cases. In the following first section, representative results will be discussed for solution convergence, method performance characteristics, and solution sensitivities (i.e., surface C_p , integrated forces and moment) to the number of iterations. The predicted surface and off-surface flow characteristics will be presented in the second section for a typical solution. A more quantitative analysis and discussion on the predicted surface pressure coefficients, forces and moment, and corresponding correlations with experimental data will be included in the third and fourth sections.

Solution Convergence and Sensitivity Characteristics

All present computations were performed on the Numerical Aerospace Simulation (NAS) Cray-C90 computer platform located at Ames Research Center. On this machine, the algorithm required about 44 μsec per iteration per cell and about 240 million words of memory for a typical computation. A sample of solution convergence characteristics is shown in figure 5 for $\alpha = 13.5^\circ$. This figure shows the \log of the total residuals (left vertical axis) and total integrated forces and moment (right vertical axis) as a function of iterations used to advance the solution. Figure 5 also shows the Courant, Friedrichs, Lewy (CFL) number strategy used to advance the solution and the total central processing unit (CPU) time requirement for the solution development. Computation for a typical solution is started from free-stream conditions with the CFL number initially set to 0.1 and subsequently ramped up linearly in two stages to a final value of 150, as shown in figure 5. All computations are performed by using

eight Cray processors. The required total CPU time for a typical computation is also shown in figure 5.

The results shown in figure 5 indicate that a nominal solution convergence apparently can be achieved with about 900 iterations, in which the total residuals are reduced about two orders of magnitude, and oscillations in the overall forces and moment are at negligible levels. However, further analyses indicated that there are clear solution sensitivities on the computed surface pressure coefficient and on forces and moment with additional solution iterations. Figure 6 shows typical solution sensitivities on computed surface pressure coefficients at eight fuselage stations (fig. 2) for three different iteration levels. Though small at this particular condition, the solution sensitivities become more pronounced at other angles of attack and are particularly reflected in the computed longitudinal aerodynamic characteristics shown in figure 7. The results shown in figure 7 clearly indicate the need for advancing the solutions to at least 1800 iterations where the solution sensitivities to further iterations become negligible. Therefore, a typical convergence characteristic plot, such as the one shown in figure 5, cannot be used solely to establish solution convergence; it is also necessary to examine at least one other figure of merit such as the surface pressure distribution, surface and off-surface flow characteristic, and surface skin friction distribution. All subsequent results presented in this report will be based on final converged solutions with 2500 iterations.

Typical Flow Features

The surface pressure coefficient contours computed at $\alpha = 13.5^\circ$, $M_\infty = 0.25$, and $R_c = 8 \times 10^6$ are shown in figure 8 for the configuration upper and lower surfaces, as well as for the computational grid in the plane of symmetry. In addition, figure 8 shows the computed total pressure contours in various cross-flow planes that coincide with fuselage stations in which the surface pressure coefficients are measured (fig. 2), along with an additional plane just aft of the wing trailing edge (FS 3000).

The flow over the wing upper surface generally can be characterized by the presence of two well-organized vortices (figs. 8(a) and (b)). The first vortex appears to form near the mid inboard wing leading

edge and is convected longitudinally downstream, roughly aft of the wing leading-edge crank. The second vortex forms over the outboard wing as the flow separates along the leading edge of the deflected flap. The low-pressure footprints associated with both vortices are clearly reflected on the surface pressure distribution contours. In addition to the two prominent wing vortices, there also appear to be two weaker vortices (i.e., lower total pressure viscous loss and higher surface pressure footprint) that form over the fuselage and roughly inboard of the inboard-wing-flap hinge line. The latter vortex originates from the wing apex region and appears to migrate downstream and coalesce with the stronger inboard wing vortex aft of the leading-edge crank near the wing trailing edge. The complex upper surface flow structures near the wing trailing edge will be discussed further in conjunction with the computed surface flow patterns. The flow over the configuration lower surface (figs. 8(c) and (d)) is characterized by a fairly benign C_p distribution ranging from ≈ 0.0 to ≈ 0.2 . In addition, the narrow band associated with the total cross-flow pressure contours over the wing lower surface can be attributed to the viscous losses within the boundary layer region.

The simulated upper surface flow pattern, superimposed over the computed surface pressure contours, is presented in figure 9. Note the slight change, relative to previous figures, in the color map (shown in gray scale) used to display the surface pressure contour. See color version at <http://techreports.larc.nasa.gov/ltrs/PDF/1999/tp/NASA-99-tp209718.pdf>. The surface flow traces are simulated by releasing particle seeds at the nodes of each surface triangle and restricting the tracing to the surface. The combination of surface C_p and surface flow results are interesting from an analysis standpoint because the connection between the surface pressure footprints for the expansion-compression regions to the vortical-flow separation line (converging streamlines) and attachment line (diverging streamlines) are highlighted. However, particular attention should be given to the interpretation of the predicted surface flow pattern caused by the inherent limitations associated with the wall function approximation. Although the predicted surface flow pattern seems plausible, it is difficult to gauge the accuracy of the predicted surface flow pattern, mainly with respect to the flow separation lines, due to the lack of complementary experimental data. With the present methodology, the

prediction of a flow separation line becomes particularly intriguing when it occurs within the boundary layer caused by the adverse pressure gradient over a smooth surface. An example of such a viscous boundary layer flow separation is clearly demonstrated and discussed in the next paragraph.

The same results as those presented in figure 9 for the surface C_p and flow pattern are shown in the middle part of figure 10 from an oblique rear vantage point, along with the computed total pressure contours in two cross-flow planes located near the wing trailing edge. No complementary experimental data exist for direct comparison with the predicted flow characteristics; however, the results shown in figure 10 are analyzed solely to demonstrate the plausibility of the computed flow structures. The total pressure contours clearly show both the inboard and outboard wing primary leading-edge vortices, along with the corresponding surface-pressure suction footprints (denoted by high-gradient regions) and the surface-flow streamline pattern. The total pressure contours at both fuselage stations indicate the presence of a weak vortex off the side of the fuselage; however, the corresponding effects on the surface pressures and the surface flow pattern (i.e., the flow separation streamline) are not discernible. Similar flow analysis over the wing indicates flow characteristics that include the primary vortex attachment (PVA) lines for both the inboard and outboard wing (i.e., attachment lines are highlighted schematically with dotted arrow-lines for both the inboard and outboard wing vortices). Also, note the complex flow pattern around the wing tip region, a massive spanwise flow around the outboard wing trailing edge, and the formation of a small vortical flow over the gap between the wing and the inboard edge of the deflected outboard trailing-edge flap (see the total pressure contour plot at FS 2790). Furthermore, it is interesting to reveal that a secondary vortex (denoted by SV in the total pressure contour plots) appears to form under the inboard wing leading-edge primary vortex with a well-defined secondary vortex separation line (denoted by SVSL in the figure). It is also important to notice that there is clearly no evidence of any local surface discontinuities that could trigger such a secondary vortex separation line. Although the prediction of such a flow characteristic with the present methodology (i.e., wall function coupled with the RANS equations) is intriguing; nevertheless, its manifestation is being reported here for the first time.

One plausible explanation for the presence of this secondary vortex separation line can be attributed to the lack of a corresponding stagnation line due to the three dimensionality of the local flow field. As a result, the application of a slip boundary condition at the surface is sufficient to capture such a secondary vortex separation line.

The simulated lower surface flow pattern, superimposed over the computed surface pressure contours, is presented in figure 11. The results generally indicate fairly benign and attached flow characteristics over the entire lower surface of the configuration. The lower surface pressure distribution also shows the expected flow compression near the deflected wing trailing-edge-flap hinge lines.

Surface Pressure Prediction and Correlation With Data

The computed surface pressure coefficients, along with the experimental measurements for $\alpha = 13.5^\circ$, $M_\infty = 0.25$, and $R_{\bar{c}} = 8 \times 10^6$, are shown at eight fuselage stations in figure 12 (see fig. 2 for fuselage stations). In an attempt to relate the pressure distribution to the configuration geometry, figure 12 also presents the corresponding geometrical cross sections for each respective fuselage station. Note that these geometric cross sections also graphically reveal the relative size of the inboard wing leading-edge radii (FS 1550 through FS 2400), as compared with the sharp leading edge on the outboard wing (FS 2660 through FS 2790). In these pressure plots, the geometry dimensions for the local semispan and the Z-coordinate are given with respect to the 0.05-scale model. In addition, no experimental surface pressure data were obtained on the fuselage; however, the numerical predictions on the fuselage portion are presented for completeness.

The computed upper surface pressure distributions at FS 1550 through FS 2010 are characterized by a narrow suction peak just aft of the wing leading edge, followed by a relatively mild flow expansion that appears to be at or just inboard of the wing-flap hinge line. The numerical results compare reasonably well with the experimental data at these three fuselage stations. The computed upper surface pressure distributions at FS 2240 and 2400 clearly indicate a wider band of low pressure that is associated with the

inboard wing leading-edge vortex, which roughly covers the entire flap local span. The leading-edge suction peak at these two fuselage stations is followed by a region of mild flow expansion, which appears to correspond to the wing apex vortex (fig. 8) inboard of the flap hinge line. The general character of the computed pressure distributions at FS 2240 and FS 2400 agrees with the experimental measurements; however, the magnitude of the suction peaks is underestimated for the wing primary leading-edge vortex. The computed surface pressure distributions over the last three fuselage stations also indicate a clear suction peak that is associated with the inboard wing primary leading-edge vortex, which appears to move slightly outboard at each consecutive fuselage station. The latter suction peaks are located at a local semispan of approximately 21, 22, and 24 in. for FS 2510, 2660, and 2790, respectively. In general, the numerical predictions for these suction peaks do not correlate well with the experimental measurements. The computed upper surface pressure distributions that are associated with the outboard wing vortex over these last three fuselage stations are predicted much better.

The computed lower surface pressure distributions at all eight fuselage stations are predicted very well except at FS 2240 and 2400. At these two stations, the disagreements between the lower surface pressure predictions and measurements are confined to the inboard section because of differences in the geometrical modeling. A possible source for this disagreement can be attributed to the geometrical differences between the numerical model and the wind tunnel model. The wind tunnel model consisted of a floor-mounted strut apparatus (fig. 1) that was not included in the numerical model. Hence, the flow expansion around the strut on the wing lower surface, causing lower surface pressure values, is not correctly simulated in the present computational study.

Similar results for the computed surface pressure coefficients and the correlations with the experimental data are presented in figures 13 and 14 for $\alpha = 9.7^\circ$ and $\alpha = 17.2^\circ$, respectively. These results are also based on the same Mach number and Reynolds number shown in figure 12. At $\alpha = 9.7^\circ$, the surface pressure correlations between the predictions and the experimental data clearly show a much better agreement than the results presented previously for $\alpha = 13.5^\circ$ at all fuselage stations. However, at

$\alpha = 17.2^\circ$ (fig. 14), the computed surface pressure distributions deviate substantially from the experimental data at all fuselage stations. With increasing angle of attack, the complex surface flow separation from the round leading edges of the inboard wing and the subsequent formation of the primary vortex system are known to be very difficult to predict, even for a simple delta wing (for an example, see ref. 23). It should be noted, however, that the surface pressure disagreements do not appear to be as severe in the region associated with the outboard wing primary leading-edge vortex and the corresponding suction peaks (i.e., FS 2510, FS 2660, and FS 2790). The favorable pressure comparison in that region can perhaps be attributed to the sharp leading-edge discontinuity, which fixes the flow separation line there, with the ensuing shear layers to form the outboard wing primary vortex.

Force and Moment Prediction and Correlation With Data

The computed longitudinal aerodynamic characteristics are presented in figure 15, along with the complementary experimental data obtained at $M_\infty = 0.25$, and $R_{\bar{c}} = 8 \times 10^6$. In general, the correlations between the predictions and experimental data are very good across the range of angles of attack. The computed lift coefficients correlate very well with the measured data for moderate angles of attack; however, they appear to be overpredicted for $\alpha \geq 13.5^\circ$. It should be noted that the computed lift- α curve exhibits a fairly linear slope, whereas the corresponding experimental data curve indicates a break in the slope near $\alpha = 5^\circ$, above which the slope is slightly less. The computed pitching moments and the drag ratios also indicate a very good agreement with the experimental data across the examined range of angles of attack, both in terms of magnitude and trends.

The computed lift-to-drag coefficients are shown in figure 16, along with the corresponding experimental data. The computational results clearly indicate an excellent agreement between the predictions and the measured data over the examined angle-of-attack range. This finding is particularly important because the C_L/C_D ratio is often considered a figure-of-merit for assessing the high-lift aerodynamic performance of a given vehicle design. Within the HSR program, for example, the lift-to-drag ratio was used as a design parameter to be maximized, at a given C_L (0.5 used for

the TCA configuration), to arrive at appropriate control surface deflections that provided the best aerodynamic performance for takeoff and landing conditions.

Concluding Remarks

Numerical viscous solutions based on an unstructured grid methodology are presented for a candidate high-speed civil transport configuration, designated as the Technology Concept Airplane (TCA) within the High-Speed Research (HSR) program. The numerical results are based on the solutions to the Reynolds average Navier-Stokes equations, coupled with a wall function, to approximate the flow within the sublayer of the turbulent boundary layer. The turbulent solutions, with the Spalart-Allmaras one-equation model, are obtained on a representative TCA high-lift configuration that consists of the fuselage and the wing with deflected full-span leading- and trailing-edge flaps. In addition to the conventional approach for assessing solution convergence, the sensitivity of the computed surface pressures, with solution development, are also shown to be a good measure for establishing a solution-convergence level of completeness.

Typical on- and off-surface flow structures, computed on a representative high-lift configuration at conditions appropriate for the takeoff and landing, indicate features that are generally plausible. The ability of the present numerical method to predict secondary vortex separation-line-flow structure is reported for the first time. The prediction of this particular flow characteristic with a wall function approximation is found to be intriguing; hence, a possible explanation is presented for its formation. Because of the lack of complementary experimental data on the flow physics, the general plausibility of the predicted flow structures is primarily established by intuitive analysis and interpretation of the measured surface pressure distributions. Such complementary experimental data on fundamental flow physics (e.g, surface flow pattern and off-surface velocity profiles) on this class of vehicles are essential ingredients used to gauge the accuracy levels of the numerical predictions.

Reasonable surface pressure correlations between the numerical results and the experimental data are obtained at $M_\infty = 0.25$ and $R_{\bar{c}} = 8 \times 10^6$ for moderate angles of attack of 9.7° and 13.5° . However, above and below these angles of attack, the correlation

between computed and measured pressure distributions start to deteriorate over the range examined in the present study. The surface pressure disagreements are shown to occur in regions that were primarily associated with the vortical flows that emanate from the round leading edge of the inboard wing. However, the predicted longitudinal aerodynamic characteristics are shown to correlate very well with existing experimental data across the examined angle-of-attack range. An excellent agreement is also obtained between the predicted lift-to-drag ratio and the experimental data over the examined range of flow conditions.

Finally, it is demonstrated that the present unstructured grid methodology is a viable engineering tool for predicting the aerodynamic performance characteristics, with reasonable accuracy, for such vehicles at typical low-speed, high-lift conditions. However, it is recommended, as part of a future effort, to plan for a focused wind tunnel test to obtain a comprehensive set of on- and off-surface flow-field data, surface pressure measurements, and force and moment data, with sufficient detail and accuracy to validate/calibrate various computational codes. Such experimental data presently do not exist for slender configurations such as the HSCT or the high-performance military class of vehicles at low speeds.

References

1. Frink, N. T.: Tetrahedral Unstructured Navier-Stokes Method for Turbulent Flows. *AIAA J.*, vol. 36, no. 11, 1998, pp. 1975–1982.
2. Anderson, W. K.; Rausch, R. D.; and Bonhaus, D. L.: Implicit/Multigrid Algorithms for Incompressible Turbulent Flows on Unstructured Grids. *J. Comput. Phys.*, vol. 128, no. 2, 1996, pp. 391–408.
3. Mavriplis, D. J.: Adaptive Meshing Techniques for Viscous Flow Calculations on Mixed Element Unstructured Meshes. AIAA-97-0857, 1997.
4. Frink, N. T.: *Tetrahedral Finite-Volume Solutions to the Navier-Stokes Equations on Complex Configurations*. NASA/TM-1998-208961, 1998.
5. Mavriplis, D. J.; and Pirzadeh, S.: Large-Scale Parallel Unstructured Mesh Computations for 3D High-Lift Analysis. AIAA-99-0537, 1999.
6. Frink, N. T.; Pirzadeh, S.; and Parikh, P.: An Unstructured-Grid Software System for Solving Complex Aerodynamic Problems. *Surface Modeling, Grid Generation, and Related Issues in Computational Fluid Dynamic (CFD) Solutions*, NASA CP-3291, 1995, pp. 289–308.
7. Frink, Neal T.; Parikh, Paresh; Pirzadeh, Shahyar: Aerodynamic Analysis of Complex Configurations Using Unstructured Grids. AIAA-91-3292, 1991.
8. Parikh, P.; Pirzadeh, S.; and Frink, N. T.: Unstructured Grid Solutions to a Wing/Pylon/Store Configuration. *J. Aircr.*, vol. 31, no. 6, 1994, pp. 1291–1296.
9. Ghaffari, Farhad: On the Vortical-Flow-Prediction Capability of an Unstructured-Grid Euler Solver. AIAA-94-0163, 1994.
10. Ghaffari, F.: *Unstructured Grid Euler Method Assessment for Longitudinal and Lateral/Directional Aerodynamic Performance Analysis of the HSR Reference H Configuration at Transonic Speeds*. NASA/TM-1999-209526, 1999.
11. Ghaffari, F.: *Unstructured Grid Euler Method Assessment for Longitudinal and Lateral/Directional Aerodynamic Performance Analysis of the HSR Technology Concept Airplane at Supersonic Cruise Speed*. NASA/TP-1999-209543, 1999.
12. Pirzadeh, S. Z.: *An Adaptive Unstructured Grid Method by Grid Subdivision, Local Remeshing, and Grid Movement*. AIAA-99-3255, 1999.
13. Heyson, Harry H.: *Linearized Theory of Wind-Tunnel Jet-Boundary Corrections and Ground Effect for VTOL-STOL Aircraft*. NASA TR R-124, 1962.
14. Roe, P. L.: Characteristic-Based Schemes for the Euler Equations. *Annual Review of Fluid Mechanics*, Volume 18, Milton van Dyke, J. V. Wehausen, and John L. Lumley, eds., Annual Reviews Inc., 1986, pp. 337–365.
15. Anderson, W. Kyle: *Grid Generation and Flow Solution Method for Euler Equations on Unstructured Grids*. NASA TM-4295, 1992.
16. Spalart, P. R.; and Allmaras, S. R.: A One-Equation Turbulence Model for Aerodynamic Flows. AIAA-92-0439, 1992.
17. White, Frank M.: *Viscous Fluid Flow*. McGraw-Hill, 1974.
18. Frink, Neal T.: Assessment of an Unstructured-Grid Method for Predicting 3-D Turbulent Viscous Flows. AIAA-96-0292, 1996.
19. Smith, Brad; and Wellington, Joan: *Initial Graphics Exchange Specification (IGES) Version 3*. U.S. Department of Commerce, National Bureau of Standards, 1986.

20. Abolhassani, J.: GRIDTOOL: A Surface Modeling and Grid Generation Tool. *Surface Modeling, Grid Generation, and Related Issues in Computational Fluid Dynamic (CFD) Solutions*, NASA CP-3291, 1995, pp. 821–832.
21. Pirzadeh, S.: Three-Dimensional Unstructured Viscous Grids by the Advancing-Layers Method. *AIAA J.*, vol. 34, no. 1, 1996, pp. 43–49.
22. Parikh, Paresh; Pirzadeh, Shahyar; and Loehner, Rainald: *A Package for 3-D Unstructured Grid Generation, Finite-Element Flow Solution and Flow Field Visualization*. NASA CR-182090, 1990.
23. Londenberg, W. Kelly: *Transonic Navier-Stokes Calculations About a 65 Degree Delta Wing*. NASA CR-4635, 1994.

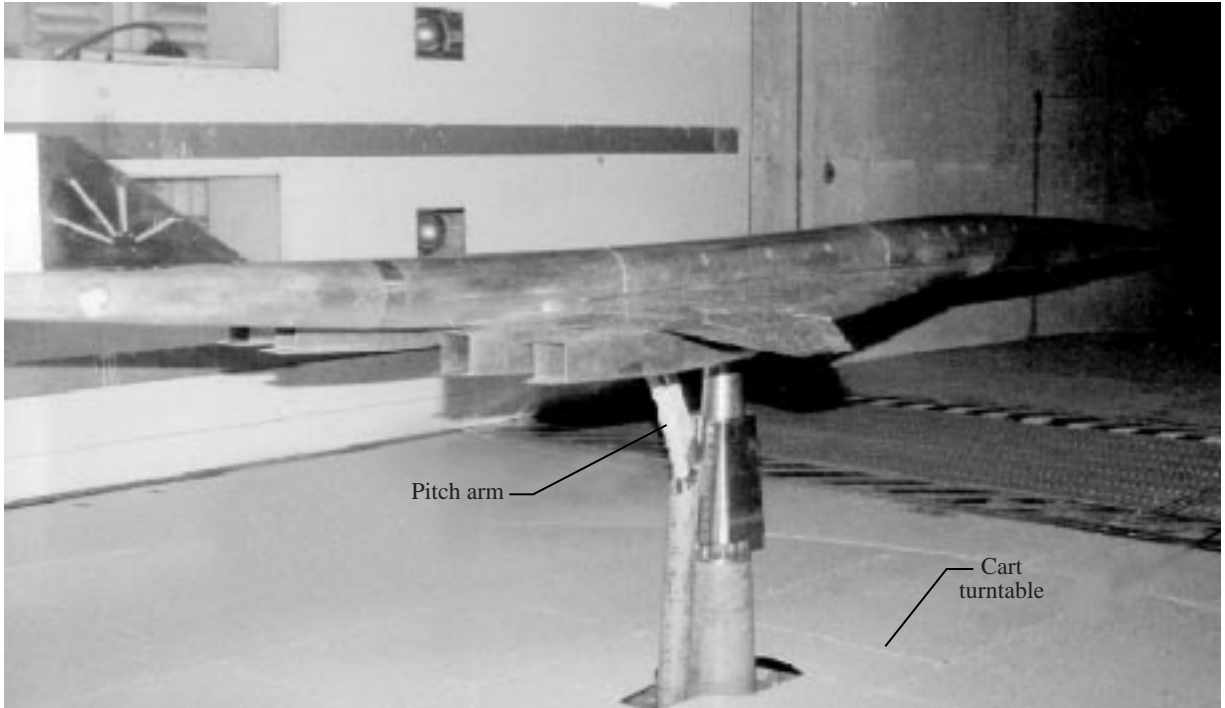


Figure 1. The 0.05-scale TCA wind tunnel model in Langley 14- by 22-Foot Tunnel.

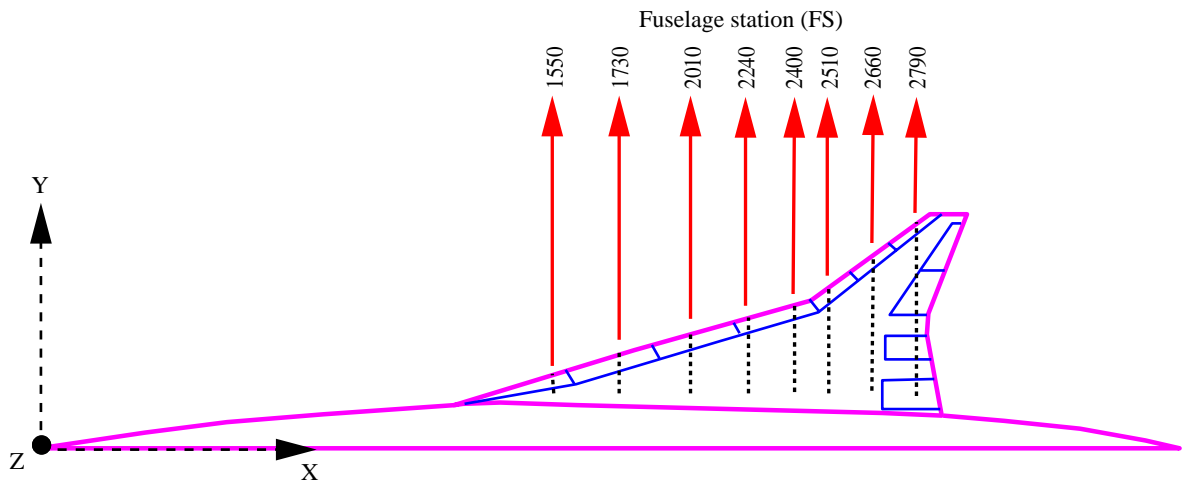
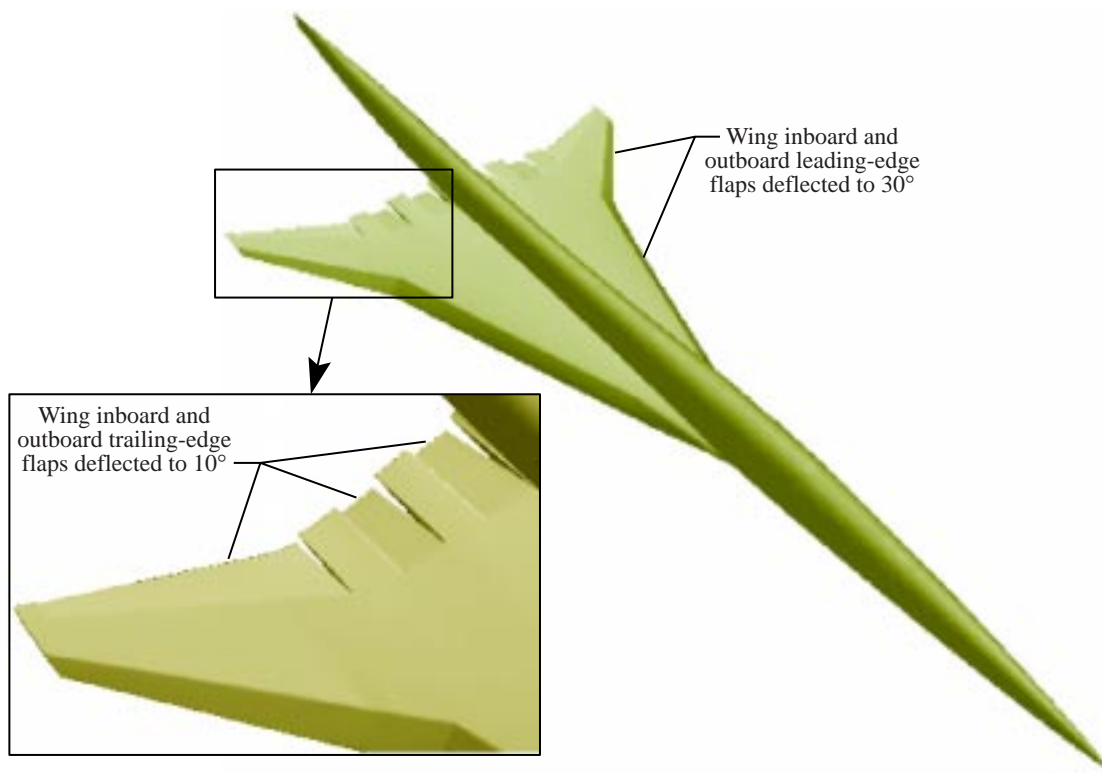


Figure 2. Schematic planform view of TCA and chordwise stations for experimental pressure measurements.

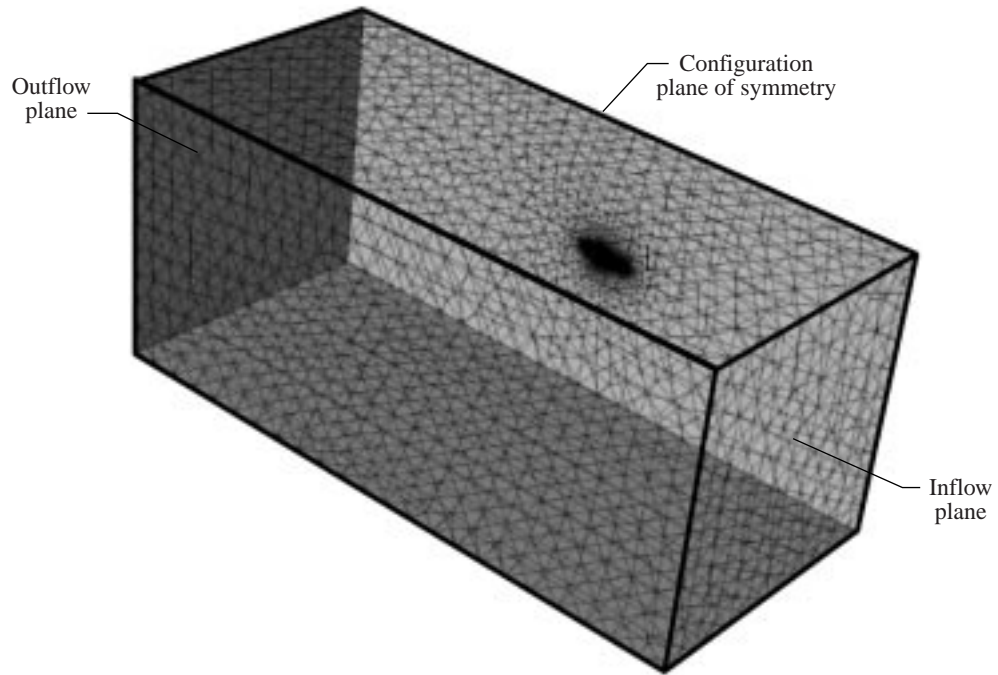


(a) Upper surface view.

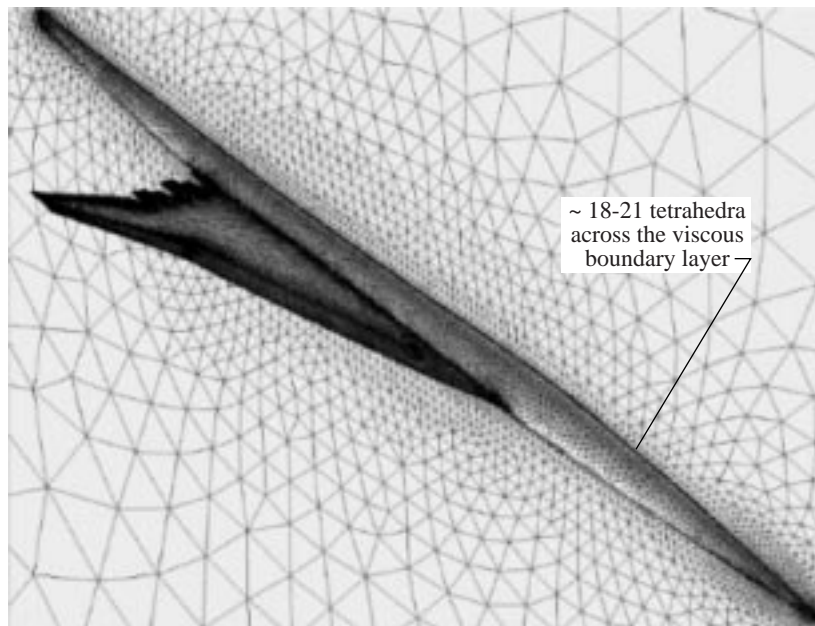


(b) Lower surface view.

Figure 3. Solid model representation of selected TCA configuration.

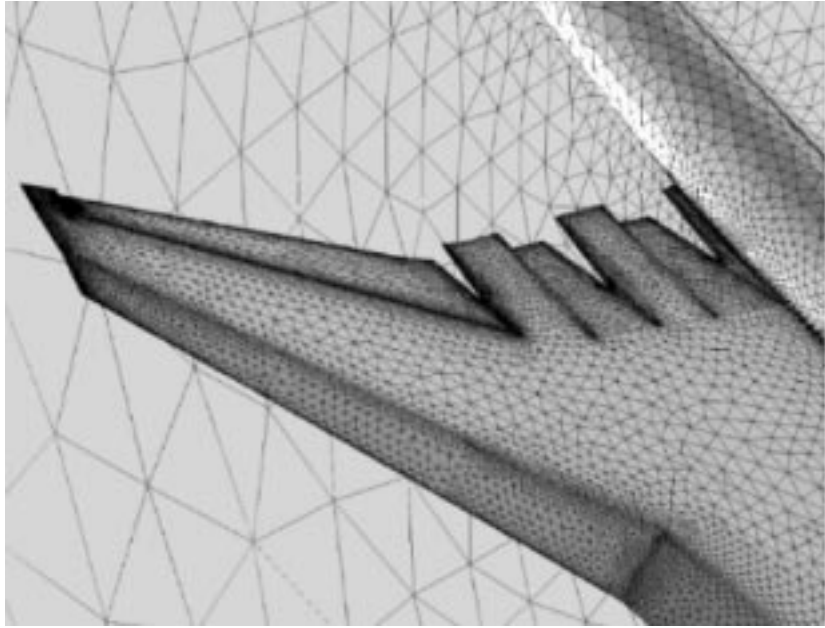


(a) Overall computational far-field boundaries.

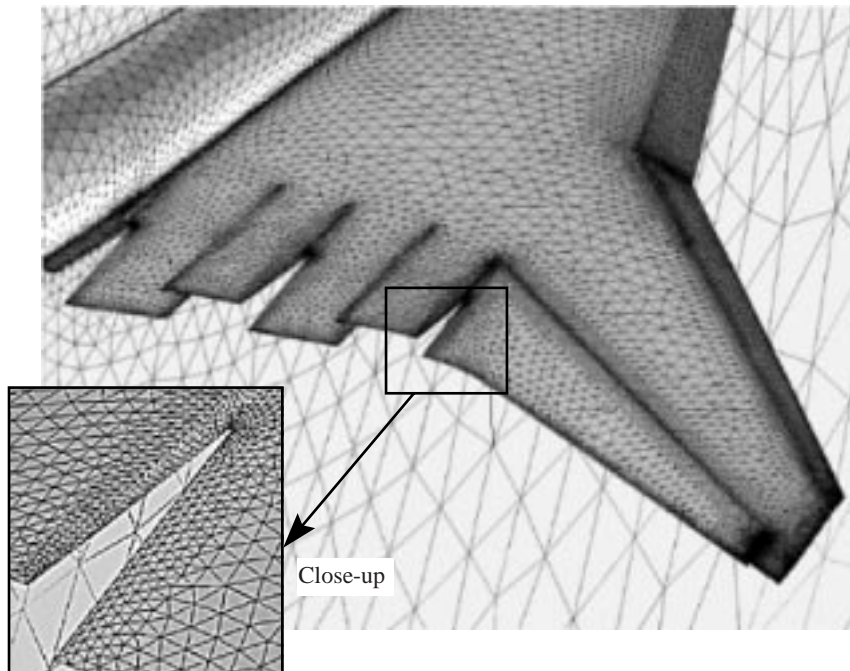


(b) Near-field view of grids on configuration upper surface and plane of symmetry.

Figure 4. Computational grid for TCA high-lift configuration.

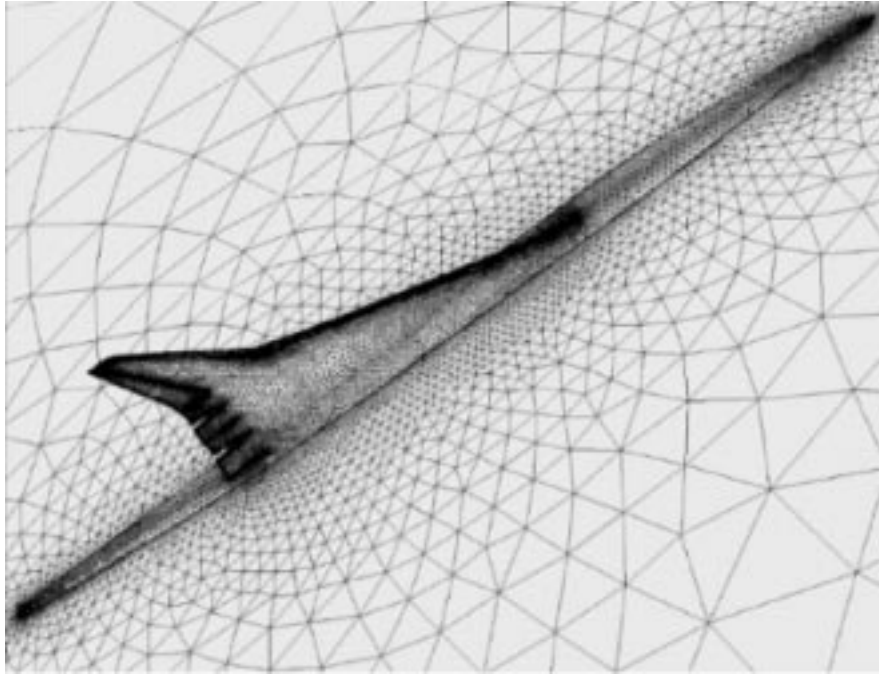


(c) Oblique front view of upper surface grids on outboard wing.

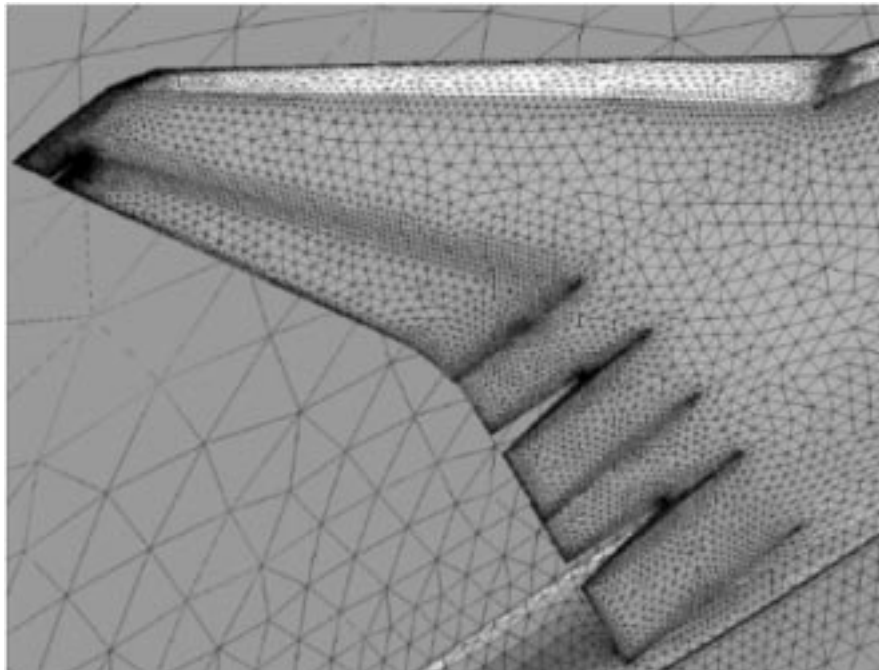


(d) Oblique rear view of upper surface grids on outboard wing.

Figure 4. Continued.



(e) Near-field view of grids on configuration lower surface and plane of symmetry.



(f) Oblique front view of grids on lower surface of outboard wing.

Figure 4. Concluded.

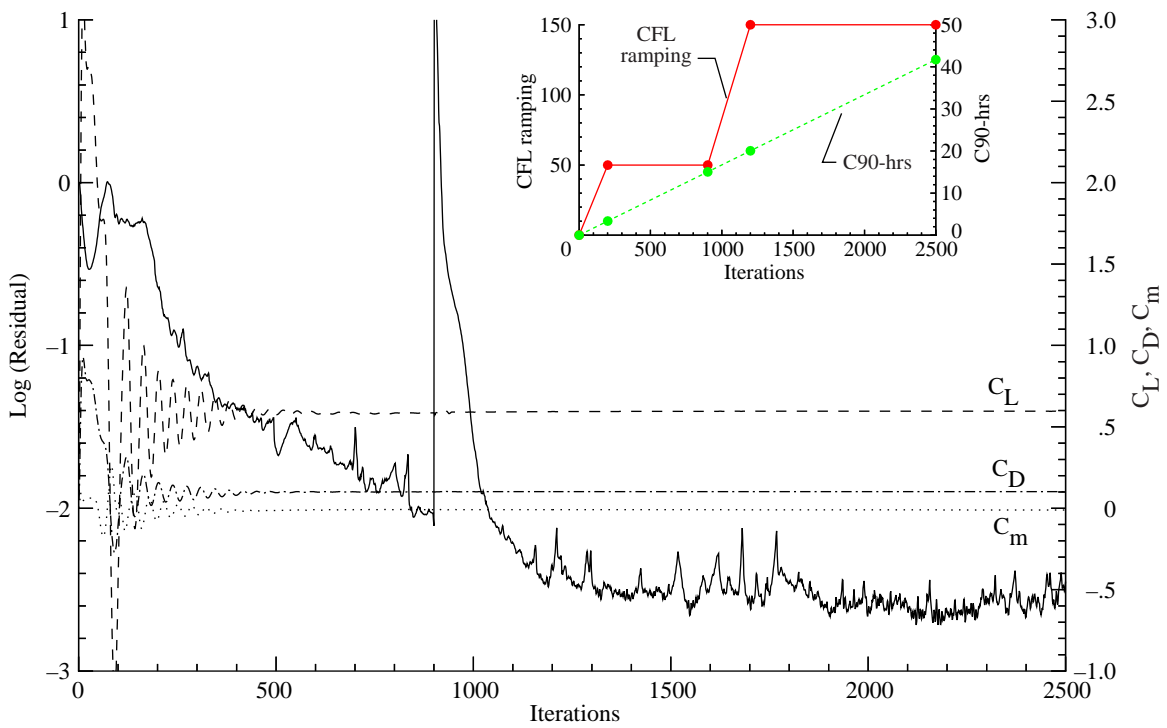
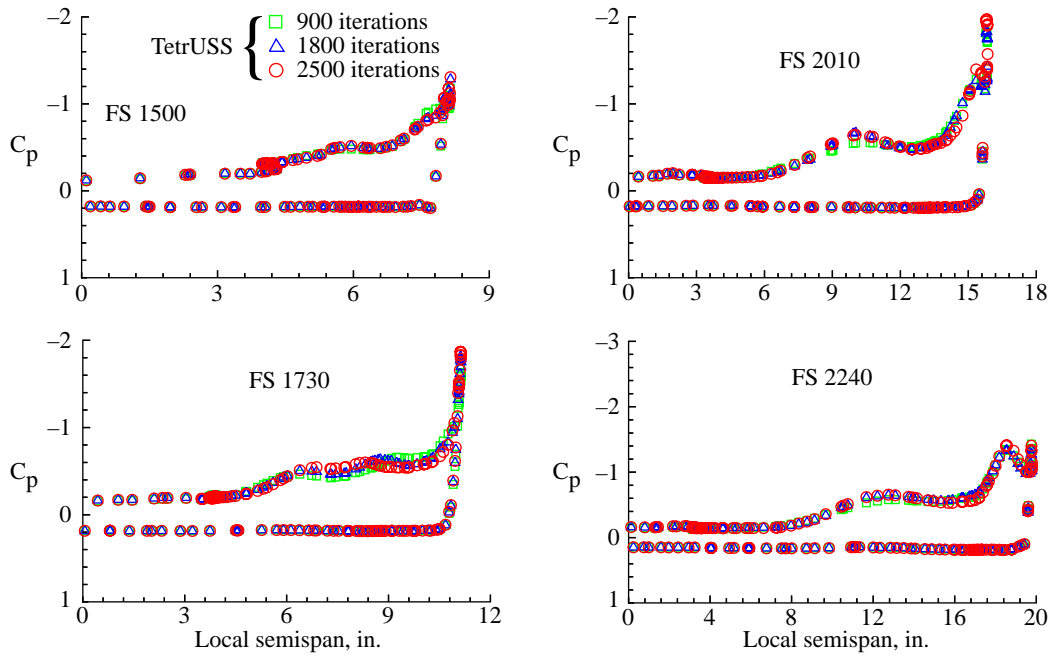
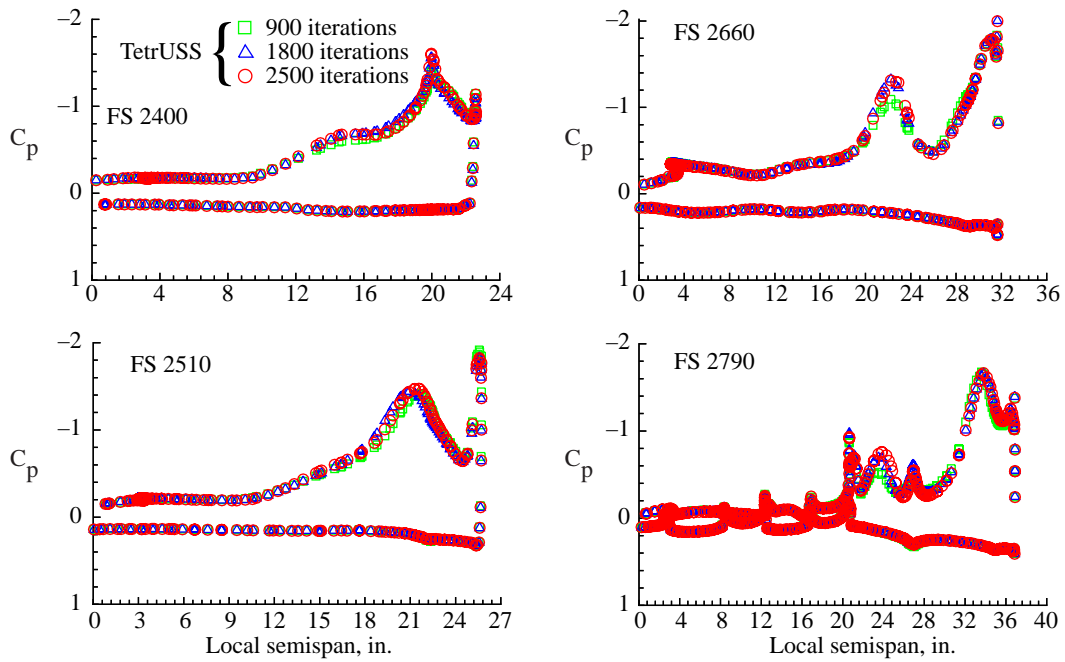


Figure 5. Typical convergence characteristics, time stepping approach, and computer resource requirements; $\alpha = 13.5^\circ$; $M_\infty = 0.25$; $R_{\bar{c}} = 8 \times 10^6$.



(a) FS 1550 through FS 2240.



(b) FS 2400 through FS 2790.

Figure 6. Effects of solution advancement on computed surface C_p ; $\alpha = 13.5^\circ$; $M_\infty = 0.25$; $R_{\bar{c}} = 8 \times 10^6$.

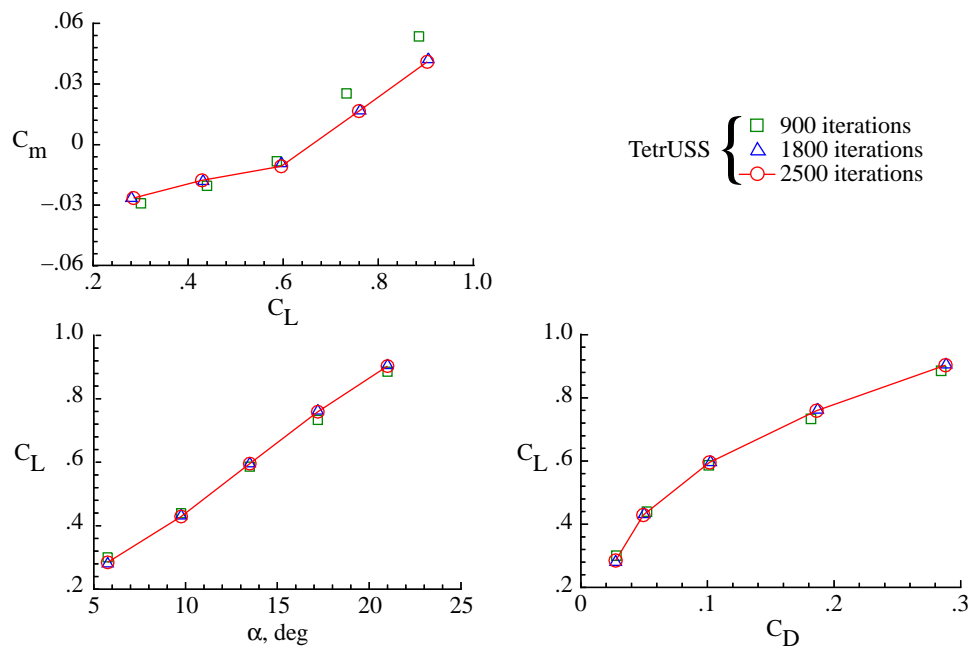
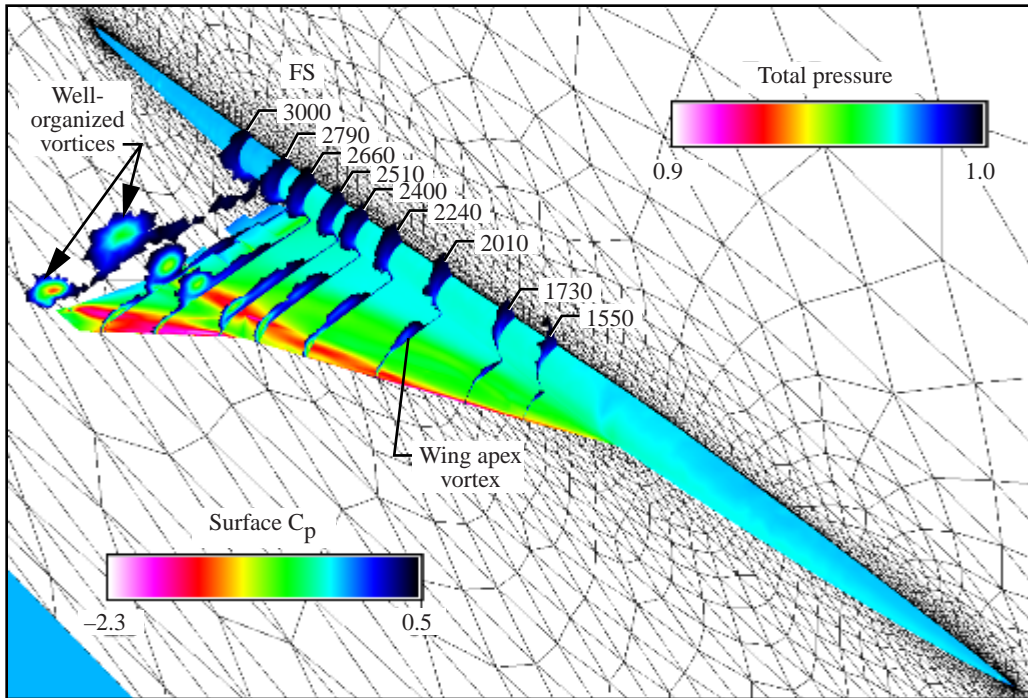
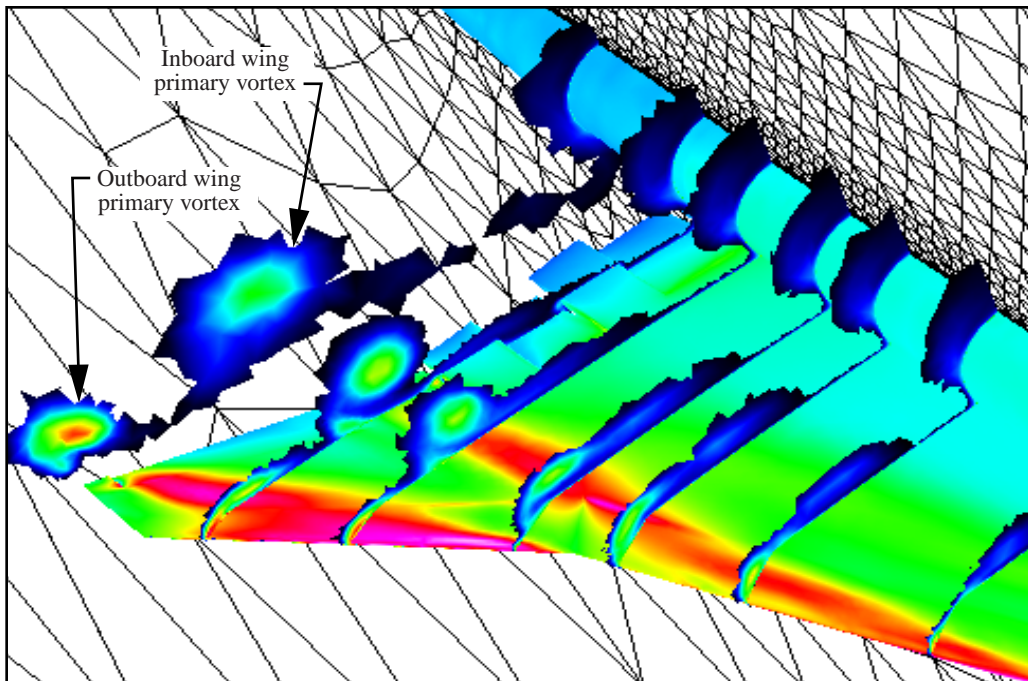


Figure 7. Effects of solution advancement on computed longitudinal characteristics.

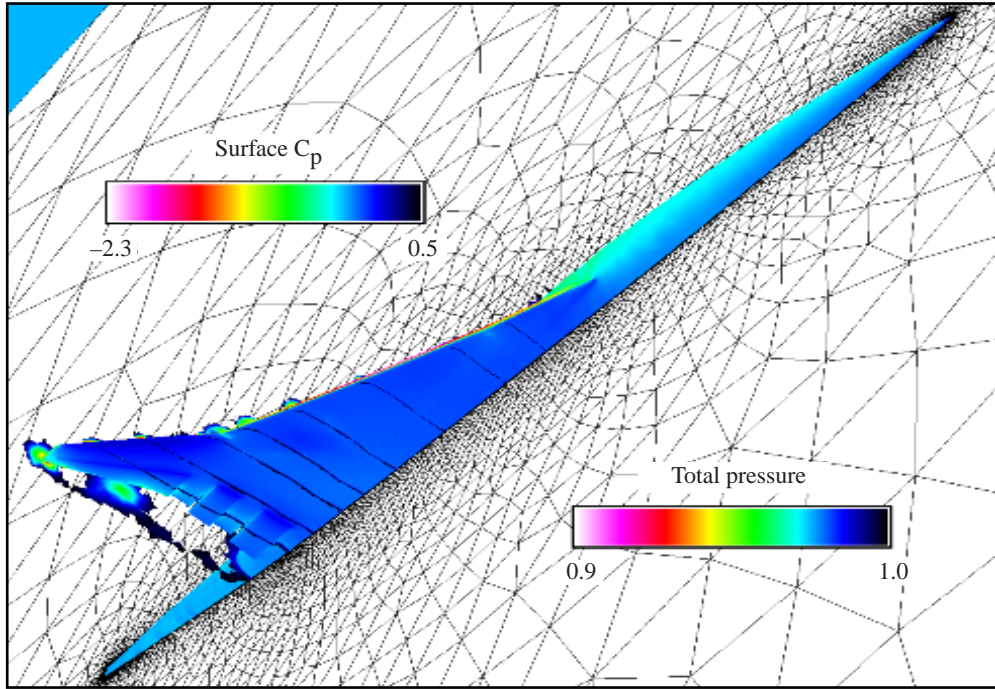


(a) Upper surface view.

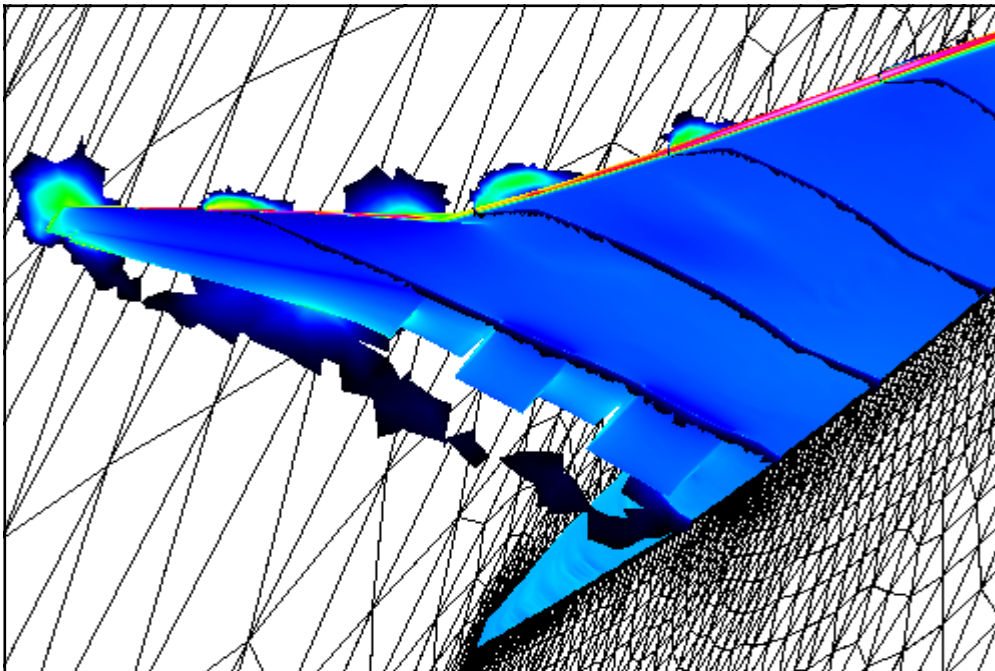


(b) Aft-wing upper surface close-up view.

Figure 8. Computed surface pressure and off-surface cross-flow total pressure contours; $\alpha = 13.5^\circ$; $M_\infty = 0.25$; $R_{\bar{c}} = 8 \times 10^6$.

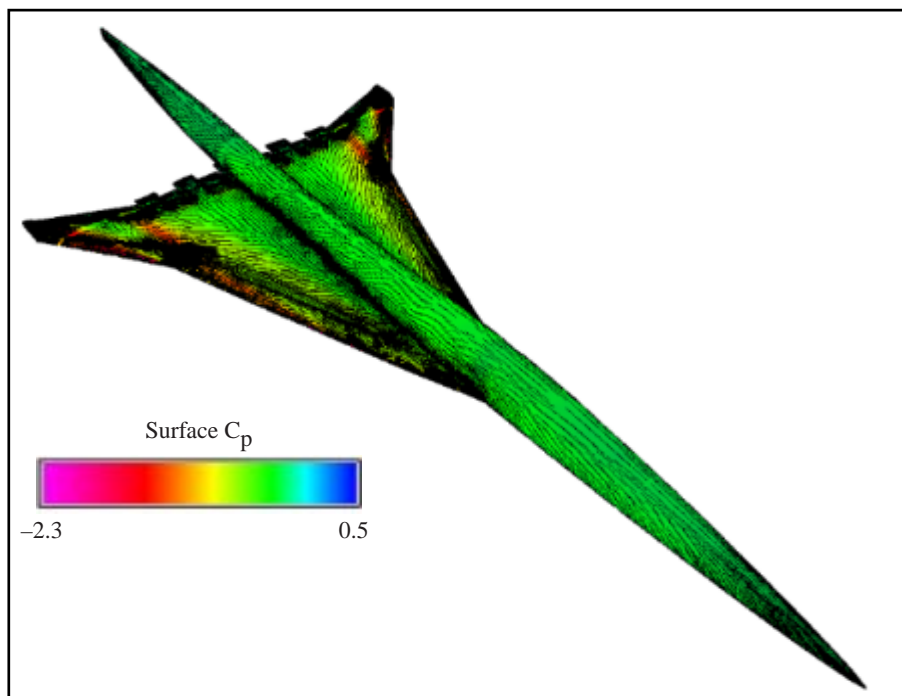


(c) Lower surface view.

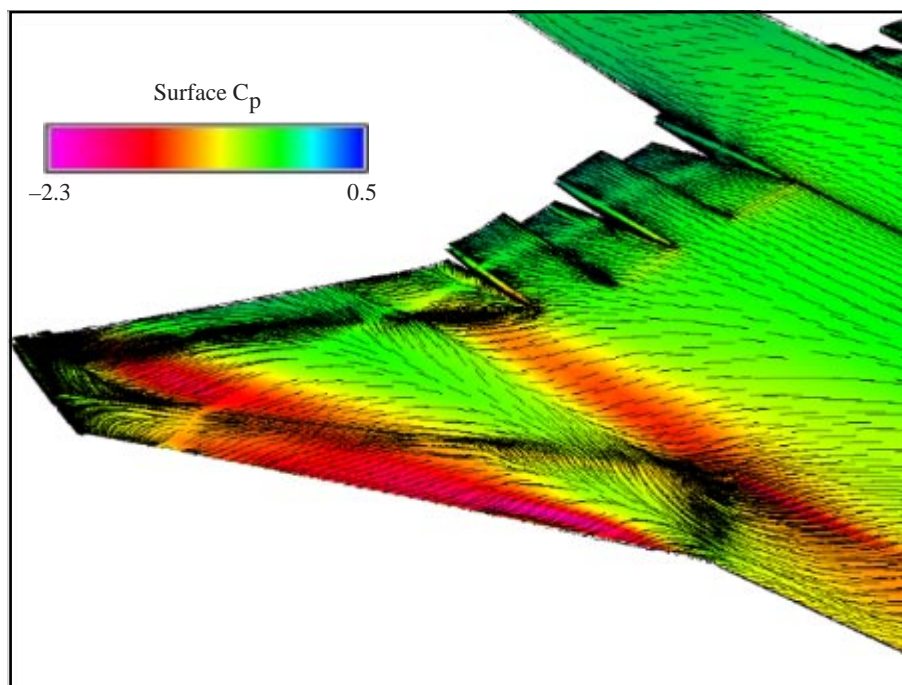


(d) Aft-wing lower surface close-up view.

Figure 8. Concluded.



(a) Upper surface view.



(b) Aft-wing upper surface close-up view.

Figure 9. Computed surface pressure coefficients and flow pattern; $\alpha = 13.5^\circ$; $M_\infty = 0.25$; $R_c = 8 \times 10^6$.

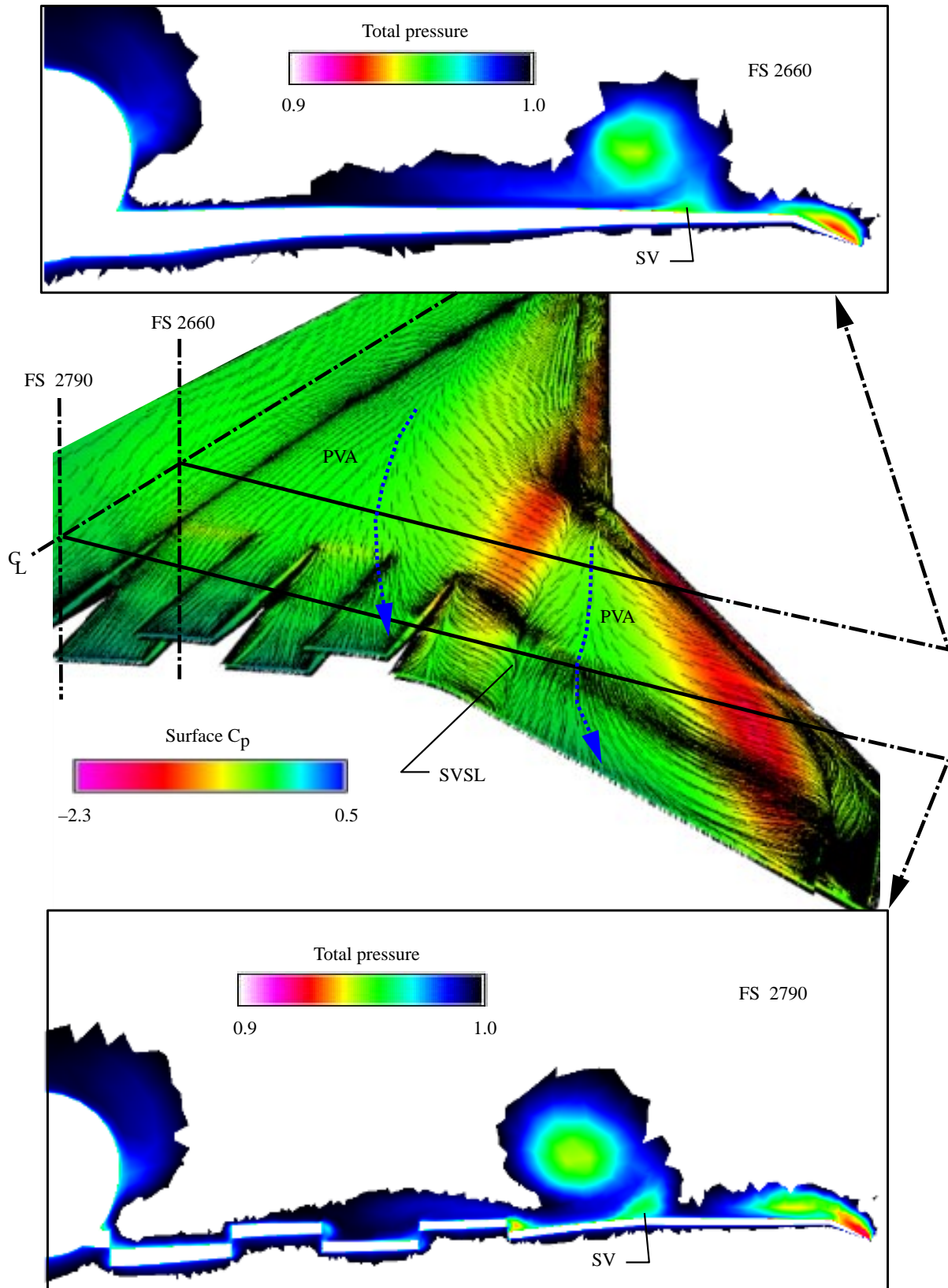
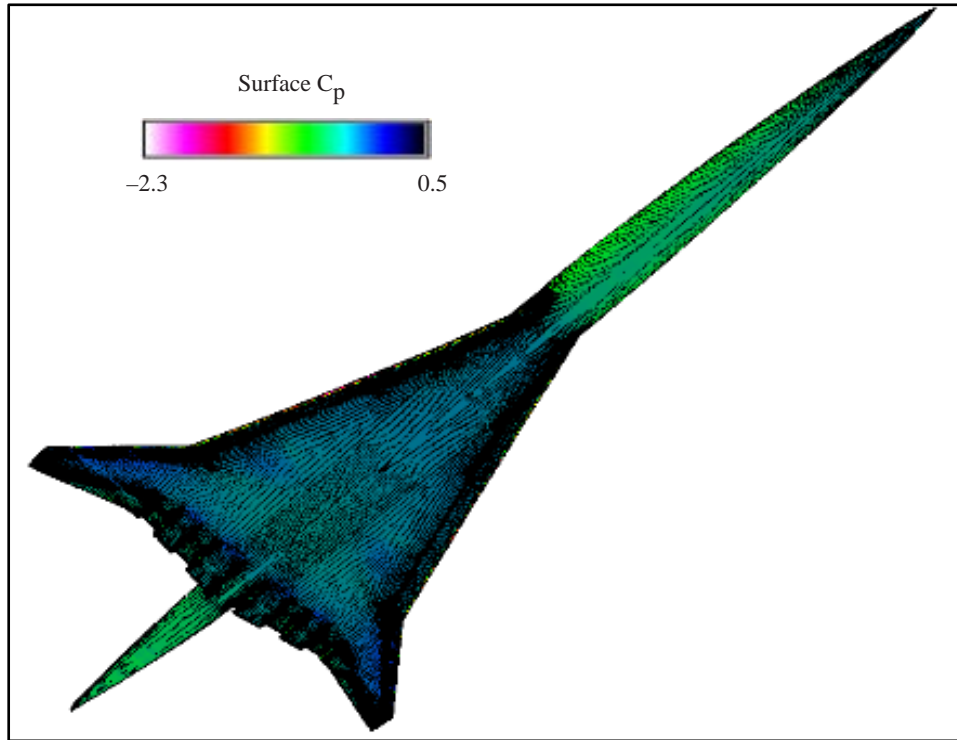
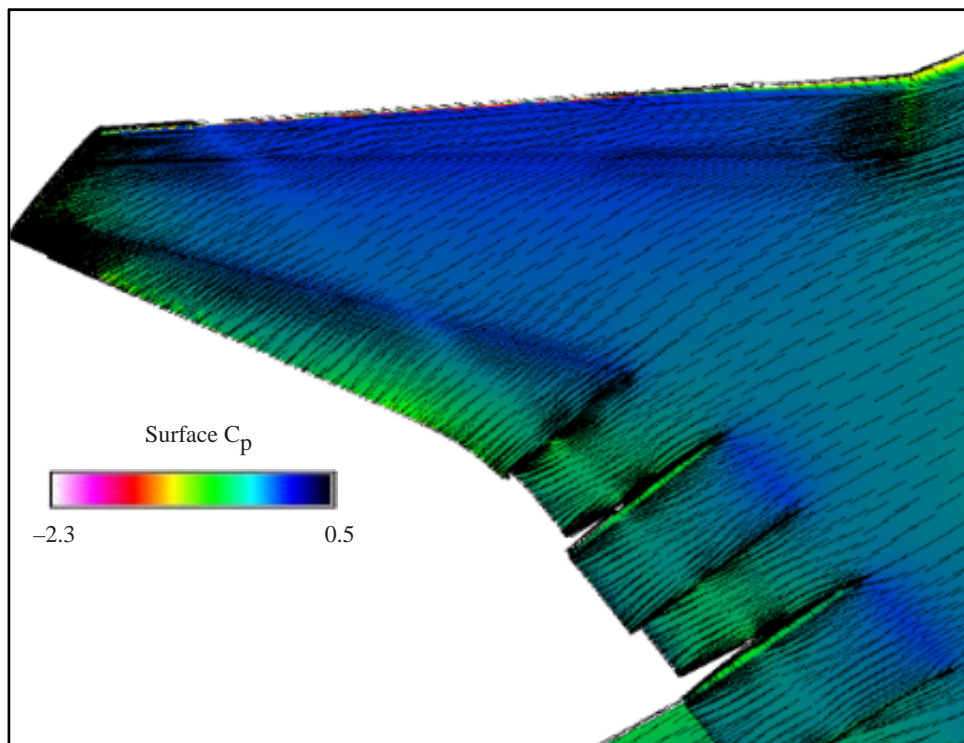


Figure 10. Computed on- and off-surface (total pressure) flow characteristics; $\alpha = 13.5^\circ$; $M_\infty = 0.25$; $R_c = 8 \times 10^6$.

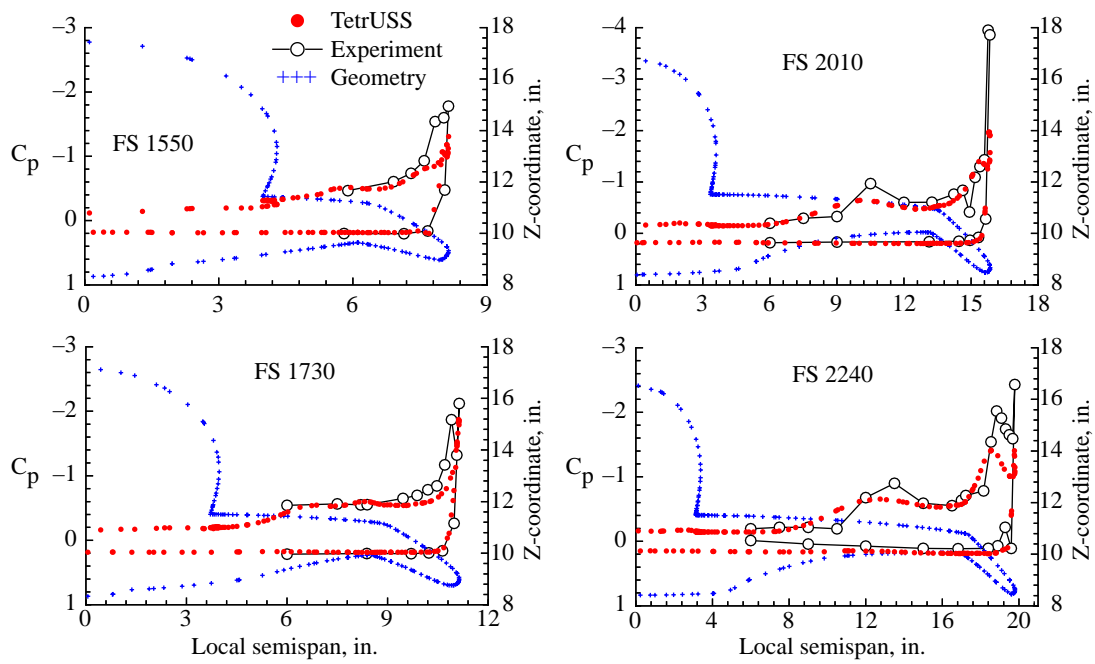


(a) Overall view.

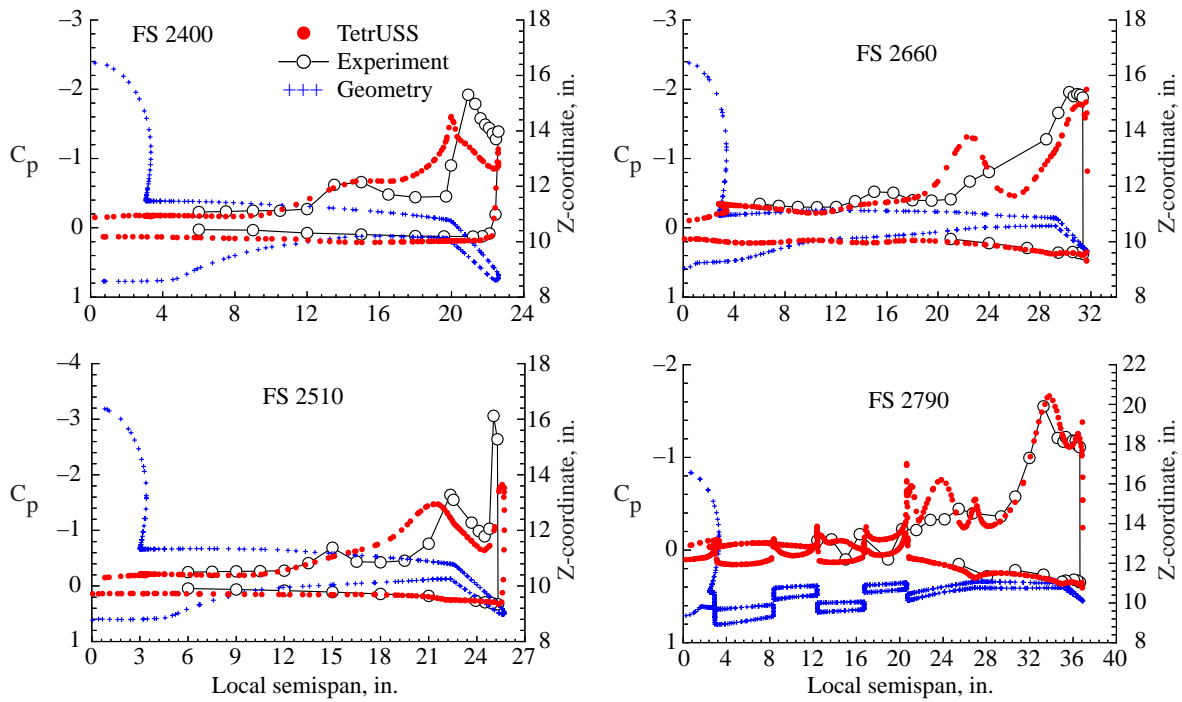


(b) Outboard wing close-up view.

Figure 11. Computed lower surface pressure coefficient and flow pattern; $\alpha = 13.5^\circ$; $M_\infty = 0.25$; $R_c = 8 \times 10^6$.

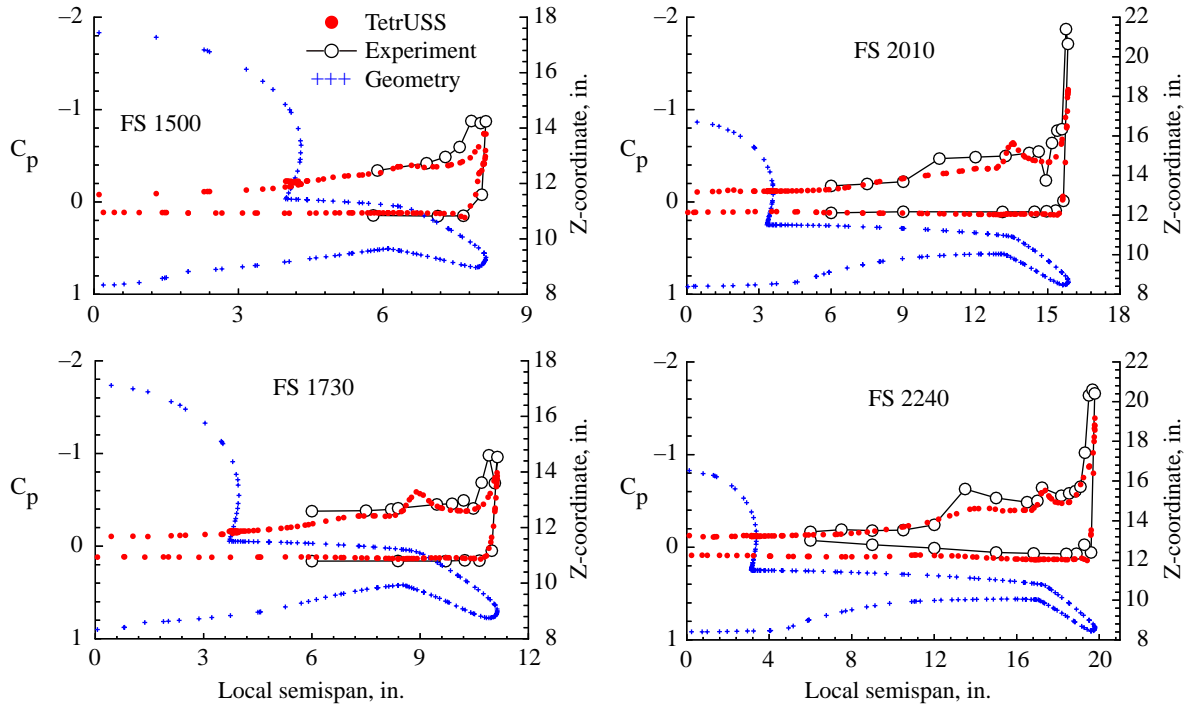


(a) FS 1550 through FS 2240.

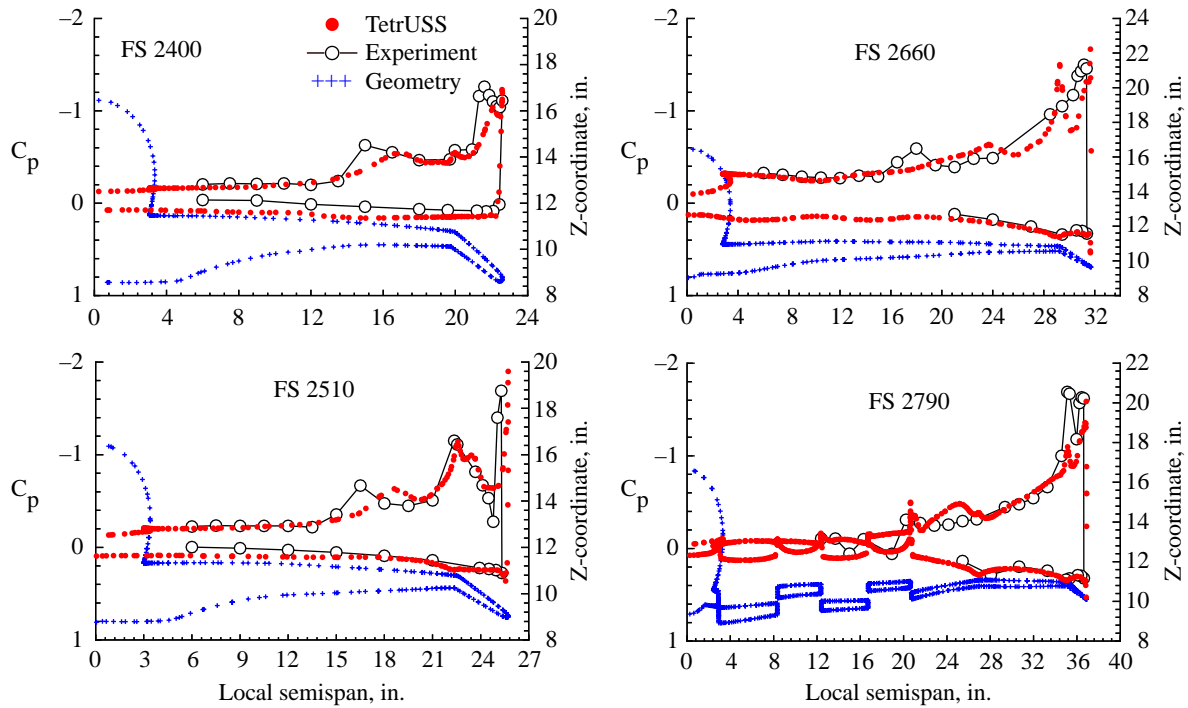


(b) FS 2400 through FS 2790.

Figure 12. Computed surface C_p and correlations with experimental data; $\alpha = 13.5^\circ$; $M_\infty = 0.25$; $R_{\bar{c}} = 8 \times 10^6$.

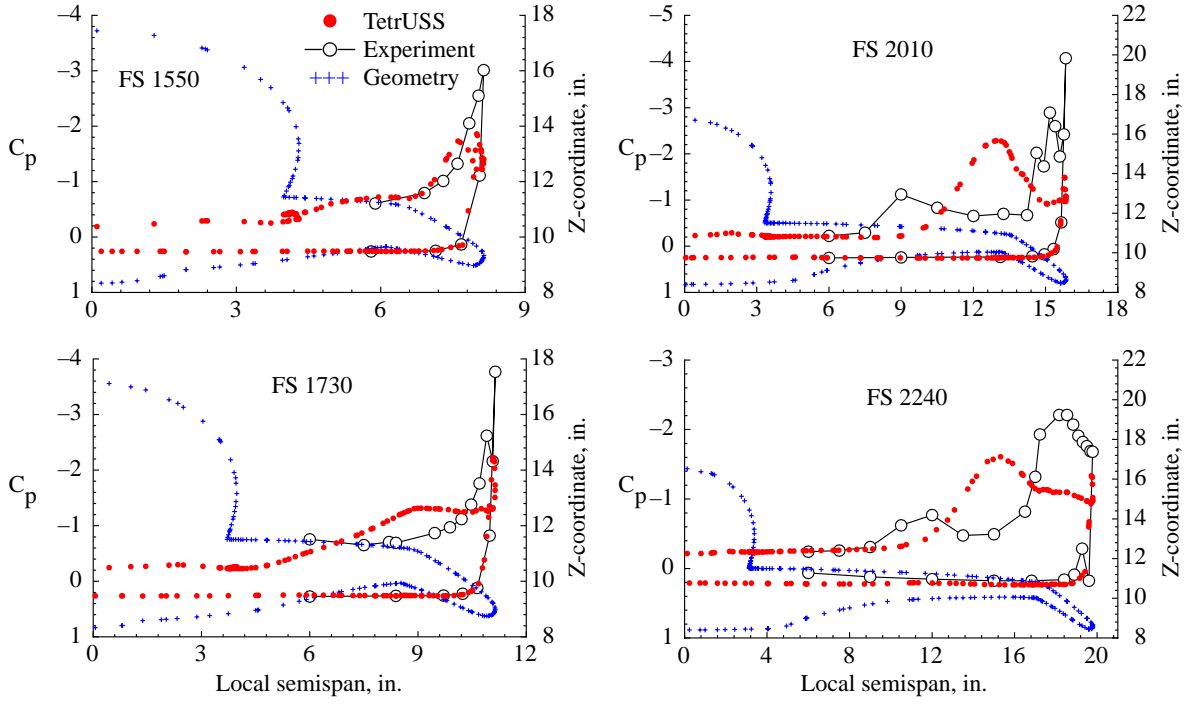


(a) FS 1550 through FS 2240.

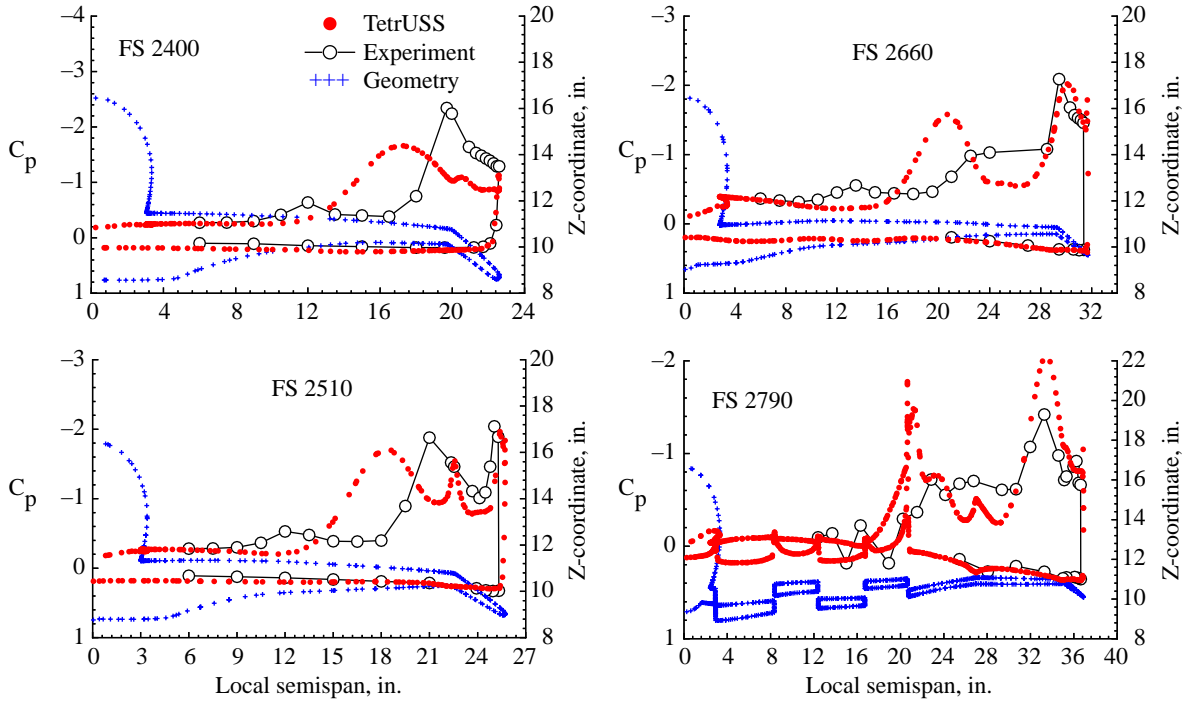


(b) FS 2400 through FS 2790.

Figure 13. Computed surface C_p and correlations with experimental data; $\alpha = 9.7^\circ$; $M_\infty = 0.25$; $R_c = 8 \times 10^6$.



(a) FS 1550 through FS 2240.



(b) FS 2400 through FS 2790.

Figure 14. Computed surface C_p and correlations with experimental data; $\alpha = 17.2^\circ$; $M_\infty = 0.25$; $R_{\bar{c}} = 8 \times 10^6$.

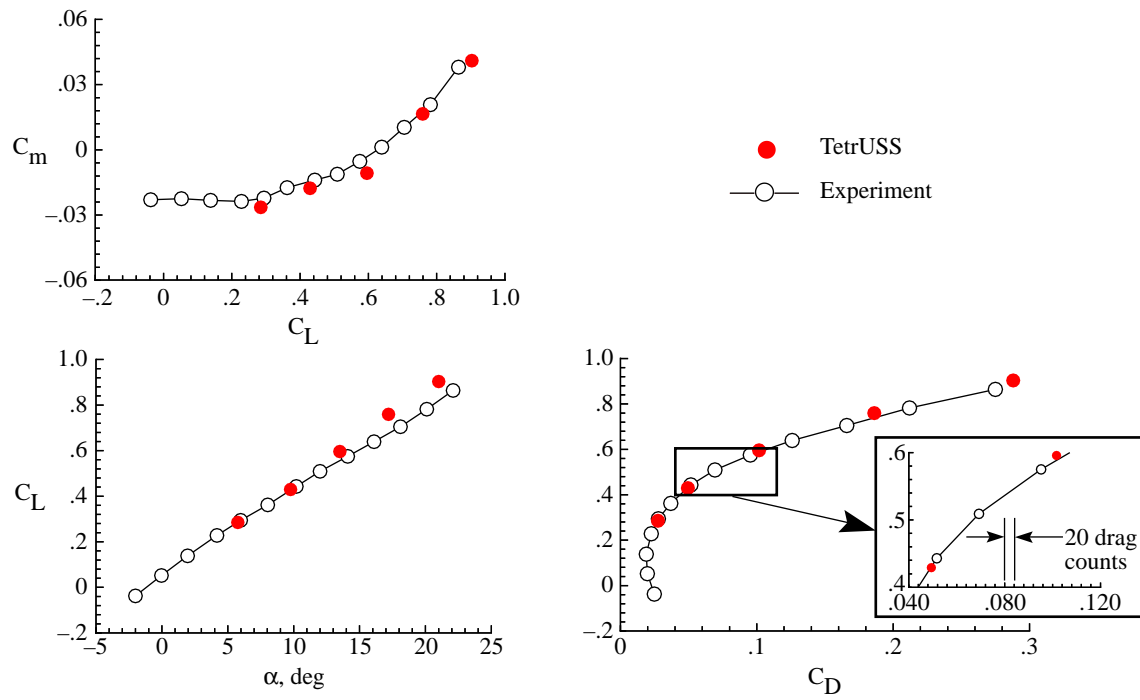


Figure 15. Computed longitudinal aerodynamics and correlations with data; $M_\infty = 0.25$; $R_{\bar{c}} = 8 \times 10^6$.

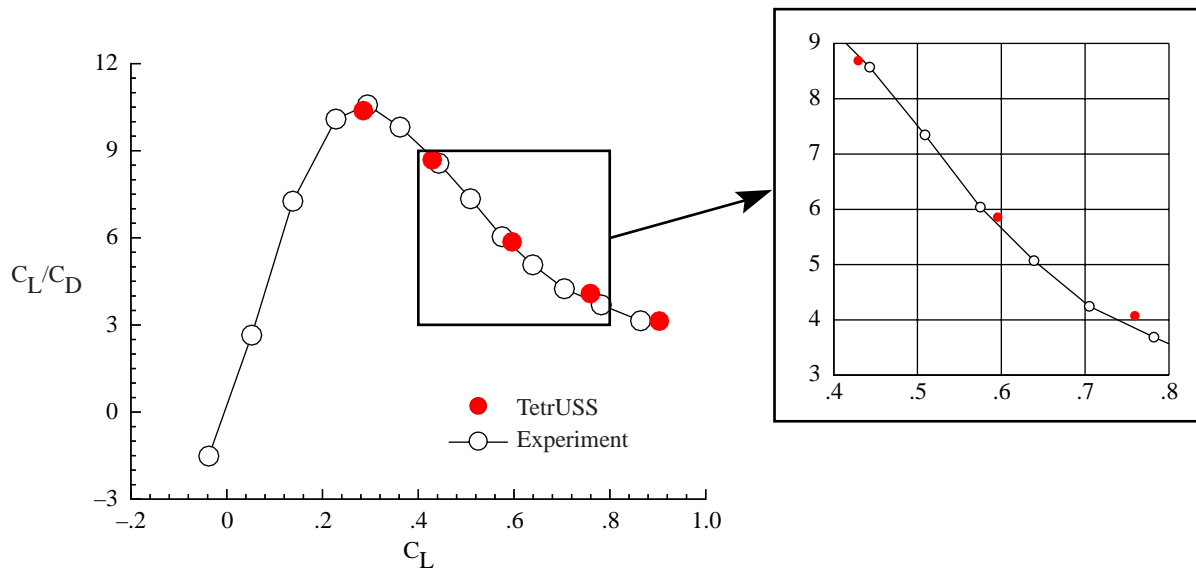


Figure 16. Computed lift over drag and correlations with experimental data; $M_\infty = 0.25$; $R_{\bar{c}} = 8 \times 10^6$.

REPORT DOCUMENTATION PAGE

Form Approved
OMB No. 07704-0188

Public reporting burden for this collection of information is estimated to average 1 hour per response, including the time for reviewing instructions, searching existing data sources, gathering and maintaining the data needed, and completing and reviewing the collection of information. Send comments regarding this burden estimate or any other aspect of this collection of information, including suggestions for reducing this burden, to Washington Headquarters Services, Directorate for Information Operations and Reports, 1215 Jefferson Davis Highway, Suite 1204, Arlington, VA 22202-4302, and to the Office of Management and Budget, Paperwork Reduction Project (0704-0188), Washington, DC 20503.

1. AGENCY USE ONLY (Leave blank)		2. REPORT DATE November 1999	3. REPORT TYPE AND DATES COVERED Technical Publication	
4. TITLE AND SUBTITLE Unstructured Grid Viscous Flow Simulation Over High-Speed Research Technology Concept Airplane at High-Lift Conditions			5. FUNDING NUMBERS WU 537-07-51-02	
6. AUTHOR(S) Farhad Ghaffari				
7. PERFORMING ORGANIZATION NAME(S) AND ADDRESS(ES) NASA Langley Research Center Hampton, VA 23681-2199			8. PERFORMING ORGANIZATION REPORT NUMBER L-17865	
9. SPONSORING/MONITORING AGENCY NAME(S) AND ADDRESS(ES) National Aeronautics and Space Administration Washington, DC 20546-0001			10. SPONSORING/MONITORING AGENCY REPORT NUMBER NASA/TP-1999-209718	
11. SUPPLEMENTARY NOTES Available electronically at the following URL address: http://techreports.larc.nasa.gov/ltrs				
12a. DISTRIBUTION/AVAILABILITY STATEMENT Unclassified-Unlimited Subject Category 02 Availability: NASA CASI (301) 621-0390			12b. DISTRIBUTION CODE	
13. ABSTRACT (Maximum 200 words) Numerical viscous solutions based on an unstructured grid methodology are presented for a candidate high-speed civil transport configuration, designated as the Technology Concept Airplane (TCA), within the High-Speed Research (HSR) program. The numerical results are obtained on a representative TCA high-lift configuration that consisted of the fuselage and the wing, with deflected full-span leading-edge and trailing-edge flaps. Typical on- and off-surface flow structures, computed at high-lift conditions appropriate for the takeoff and landing, indicated features that are generally plausible. Reasonable surface pressure correlations between the numerical results and the experimental data are obtained at free-stream Mach number $M_\infty = 0.25$ and Reynolds number based on \bar{c} $R_c = 8 \times 10^6$ for moderate angles of attack of 9.7° and 13.5° . However, above and below this angle-of-attack range, the correlation between computed and measured pressure distributions starts to deteriorate over the examined angle-of-attack range. The predicted longitudinal aerodynamic characteristics are shown to correlate very well with existing experimental data across the examined angle-of-attack range. An excellent agreement is also obtained between the predicted lift-to-drag ratio and the experimental data over the examined range of flow conditions.				
14. SUBJECT TERMS Computational fluid dynamics; Unstructured grid viscous flows; Wall function approximation; High-Speed Civil Transport; High-lift aerodynamics			15. NUMBER OF PAGES 32	
			16. PRICE CODE A03	
17. SECURITY CLASSIFICATION OF REPORT Unclassified	18. SECURITY CLASSIFICATION OF THIS PAGE Unclassified	19. SECURITY CLASSIFICATION OF ABSTRACT Unclassified	20. LIMITATION OF ABSTRACT UL	